








An Explanation of GRB Fermi-LAT Flares and High-Energy Photons in Stratified Afterglows

Nissim Fraija ^{1,*}, Boris Betancourt Kamenetskaia ^{2,3}, Antonio Galván-Gómez ¹, Peter Veres ^{4,5}, Rosa L. Becerra ⁶, Simone Dichiara ⁷, Maria G. Dainotti ^{8,9,10}, Francisco Lizcano¹, Edilberto Aguilar-Ruiz¹

¹*Instituto de Astronomía, Universidad Nacional Autónoma de México, Circuito Exterior, C.U., A. Postal 70-264, 04510 México City, México*

²*Technical University of Munich, TUM School of Natural Sciences, Physics Department, James-Frank-Str 1, 85748 Garching, Germany*

³*Max-Planck-Institut für Physik (Werner-Heisenberg-Institut), Föhringer Ring 6, 80805 Munich, Germany*

⁴*Department of Space Science, University of Alabama in Huntsville, Huntsville, AL 35899, USA*

⁵*Center for Space Plasma and Aeronomic Research, University of Alabama in Huntsville, Huntsville, AL 35899, USA*

⁶*Instituto de Ciencias Nucleares, Universidad Nacional Autónoma de México, Apartado Postal 70-264, 04510 México, CDMX, México*

⁷*Department of Astronomy and Astrophysics, The Pennsylvania State University, 525 Davey Lab, University Park, PA 16802, USA*

⁸*National Astronomical Observatory of Japan, 2-21-1 Osawa, Mitaka, Tokyo 181-8588, Japan*

⁹*Space Science Institute, Boulder, CO, USA*

¹⁰*The Graduate University for Advanced Studies, SOKENDAI, Shonankokusaimura, Hayama, Miura District, Kanagawa 240-0193, Japan*

Accepted XXX. Received YYY; in original form ZZZ

ABSTRACT

The second *Fermi*/LAT gamma-ray burst (GRB) catalog (2FLGC) spanning the first decade of operations by the LAT collaboration was recently released. The closure relations of the synchrotron forward shock (FS) model are not able to reproduce a sizeable portion of the afterglow-phase light curves in this collection, indicating that there may be a large contribution from some other mechanism. Recently, synchrotron self-Compton (SSC) light curves from the reverse shock (RS) regions were derived in the thick- and thin-shell regime for a constant-density medium, and it was demonstrated that analytical light curves could explain the GeV flare observed in several bursts from 2FLGC, including GRB 160509A. Here, we generalise the SSC RS scenario from the constant density to a stratified medium, and show that this contribution helps to describe the early light curves exhibited in some *Fermi*/LAT-detected bursts. As a particular case, we model a sample of eight bursts that exhibited a short-lasting emission with the synchrotron and SSC model from FS and RS regions, evolving in a stellar-wind environment, constraining the microphysical parameters, the circumburst density, the bulk Lorentz factor, and the fraction of shock-accelerated electrons. We demonstrate that the highest-energy photons can only be described by the SSC from the forward-shock region.

Key words: gamma-rays bursts: individual: [GRB 080916C, 090323, 090902B, 090926A, 110731A, 130427A, 160625B, 180720B] – radiation mechanism: non-thermal – acceleration of particles

1 INTRODUCTION

Gamma-ray bursts (GRBs) are among the most powerful short-duration explosions in the universe. These sources are often discovered as transient gamma-ray flashes that last from milliseconds to hours and emit $\sim 10^{51} - 10^{54}$ erg (for a review, see Kumar & Zhang 2015). Most GRBs are usually detected in the keV–MeV energy range, and their classification is determined by the duration of the first event called "prompt emission" (T_{90}).¹ Typically, GRBs are modelled by the empirical Band function (Band et al. 1993). After the first event, a second event, known as afterglow, is observed from radio wavelengths up to TeV gamma-rays and is explained using the fireball scenario (e.g., see Cavallo & Rees 1978). When a relativistic jet comes into contact with the circumburst medium, the basic model predicts the formation of two shock waves: a forward shock (FS; Kobayashi et al. 1999; Granot & Sari 2002; Sari et al. 1998; Becerra et al. 2019a) and a reverse shock (RS; Kobayashi 2000; Kobayashi & Zhang 2003; Fraija et al. 2016; Becerra et al. 2019b). Both shocks are predicted to produce synchrotron and synchrotron-self Compton (SSC) photons due to the acceleration and cool down of the non-thermal electron distribution. Synchrotron photons are scattered to energies larger than tens of GeV by the SSC process (Zhang & Mészáros 2001; Fraija et al. 2019b), even if the highest photon energy produced by the synchrotron process is $\sim 5 - 10$ GeV (Piran & Nakar 2010; Abdo et al. 2009b; Barniol Duran & Kumar 2011).

* E-mail: nifraija@astro.unam.mx

¹ T_{90} represents the time during which a GRB emits between 5% and 95% of the total observed counts from its prompt emission.

According to multi-wavelength data modelling during the afterglow phase, multiple GRBs are compatible with a circumburst medium with a density profile $\propto r^{-k}$ with a PL index in the range $0 \leq k < 3$. For example, Yi et al. (2013) studied the evolution of the FS and RS emission in a circumstellar medium represented by $\propto r^{-k}$. They tested their afterglow model on 19 bursts and found that the density profile index ranged from $0.4 \leq k \leq 1.4$. Liang et al. (2013), who examined a larger sample of 146 bursts, reported a range consistent with Yi et al.'s result. Since black hole accretion of a stellar envelope produces the plateau phase in X-ray light curves, Kumar et al. (2008) constructed a density profile index with $k > 2$. Using a synchrotron afterglow model in the adiabatic domain without energy injection, Kouveliotou et al. (2013) evaluated the multiwavelength data of GRB 130427A, one of the most intense bursts with redshift $z < 1$. The authors concluded that these observations were consistent with a density profile index that ranged between $k = 0$ (constant-density medium) and $k = 2$ (wind-like medium). Izzo et al. (2020) modelled the X-ray observations of the nearby SN 2020bvc. According to the authors, these afterglow observations were consistent with synchrotron emission evolving in a circumburst medium with a density profile index of $k = 1.5$. A complete analysis of *Fermi* and Swift observations by Ajello et al. (2018); Cenko et al. (2011); Ackermann et al. (2013b) found that there is a preference for LAT-detected bursts to evolve in a wind-like circumstellar medium. This inference was due to the observed behaviour of the cooling frequency in the synchrotron spectrum in several GRBs. It was noted that it evolved in time to larger energies, a behaviour that contrasted with the predicted evolution to lower energies, as expected from a constant-density medium. As such, the afterglow was best fitted with a low-density wind-like model (Ajello et al. 2018). The bursts in question were GRB 090323, GRB 090328, GRB 090902B, GRB 090926A (Cenko et al. 2011), and GRB 110731A (Ackermann et al. 2013b).

Ajello et al. (2019) presented the Second *Fermi*/LAT GRB Catalogue (2FLGC), covering the first decade of operations (from 2008 to 2018, August 4). The data set contains 169 bursts with high-energy emissions greater than 100 MeV, including 29 bursts higher than 10 GeV. Additionally, this data set includes a sample of 86 bursts with temporarily extended emission described with a power law (PL) function and a broken power law (BPL) function. A subset of these events (21 GRBs) showed a break in the LAT light curve between 63 and 1250 s. Although long-lasting emission is commonly interpreted as synchrotron radiation from external FSs (Kumar & Barniol Duran 2009, 2010), not all LAT light curves fulfil the relation between the temporal and spectral indices' evolutions or the closure relations predicted if the FS dominates the emission (Sari et al. 1998). Furthermore, data suggests that the entire GeV light curve for multiple bursts cannot be satisfactorily described by FS synchrotron radiation alone (Maxham et al. 2011).

Fraija et al. (2020) derived the SSC light curves from the RS region for a constant-density medium. They demonstrated that analytical SSC light curves from the RS region could explain the GeV flares observed in several bursts from 2FLGC. The late-time steepening of LAT afterglow observations was caused by the synchrotron cooling break passing across the LAT energy band when the FS evolves in a uniform environment. Here, we generalise the SSC light curves from the RS for a uniform-density medium to a stratified environment with a profile density $\propto r^{-k}$ with k lying in the range of $0 \leq k < 3$. The paper is structured as follows: in Section §2, we derive the SSC light curves evolving in a stratified medium. Section §3 presents the analysis of *Fermi*/LAT data, the derivation of the *Fermi*/LAT light curves and the modelling of the multiwavelength observations of a sample of eight GRBs with our current model for $k = 2$. In addition, we present the results and a discussion. Section §4 provides a summary of our work and some concluding remarks. We use unprimed (primed) quantities in the observer (comoving) frame. The subindexes “f” and “r” refer to the quantities derived in the FS and RS regions, respectively.

2 SSC LIGHT CURVES FROM THE REVERSE SHOCK EVOLVING IN A STRATIFIED ENVIRONMENT

When the relativistic jet encounters the stratified medium, a RS is formed, and it propagates back into the outflow (Mészáros & Rees 1997; Sari & Piran 1999; Kobayashi & Sari 2000). We consider a density profile of the stratified medium $n(r) = A_k r^{-k}$ with $0 \leq k < 3$, and use the value of $A_k = \frac{\dot{M}_W}{4\pi m_p v_W} A_k = 3.0 \times 10^{35} \text{ cm}^{-1} A_k$ for $k = 2$ to report the quantities of the theoretical model, unless otherwise indicated. The terms v_W and \dot{M}_W correspond to the wind velocity and the mass-loss rate, respectively, m_p is the proton mass, and A_k is the density parameter. The evolution of the bulk Lorentz factor is estimated as $\Gamma = \left(\frac{\ell}{\Delta}\right)^{\frac{3-k}{2(4-k)}}$, where $\ell = \left(\frac{(3-k)E}{4\pi m_p c^2 A_k}\right)^{\frac{1}{3-k}}$ and $\Delta = 2c(1+z)^{-1} t_x$ are the Sedov length and the observed width of the shell, respectively.² The dynamics of the RS is categorized into two distinct scenarios: the thick-shell regime for $\Gamma_c \lesssim \Gamma$ or $t_x \lesssim T_{90}$, and in the thin-shell regime for $\Gamma < \Gamma_c$ or $T_{90} < t_x$, where Γ_c is the critical Lorentz factor, which is calculated considering the evolution of the bulk Lorentz factor evaluated at the duration of the burst ($\Gamma_c \equiv \Gamma(t_x = T_{90})$). In this case, the critical Lorentz factor becomes

$$\Gamma_c \equiv \left(\frac{3-k}{(4c)^{5-k} \pi m_p}\right)^{\frac{1}{2(4-k)}} (1+z)^{\frac{3-k}{2(4-k)}} E^{\frac{1}{2(4-k)}} A_k^{-\frac{1}{2(4-k)}} T_{90}^{-\frac{3-k}{2(4-k)}}. \quad (1)$$

² The term t_x is the shock crossing time, z is the redshift, and c is the speed of light. The isotropic gamma-ray energy, $E_{\gamma, \text{iso}}$, determines the isotropic equivalent kinetic energy, E , through the kinetic efficiency $\eta = E_{\gamma, \text{iso}} / (E + E_{\gamma, \text{iso}})$.

2.1 Dynamics of the thick-shell scenario

The RS in the thick-shell scenario is ultra-relativistic and can decelerate the shell dramatically. Before the RS crosses the shell, the scale of the hydrodynamic quantities as a function of the observed time is $\gamma_3 \propto t^{-\frac{2-k}{2(4-k)}}$, $n_3 \propto t^{-\frac{k+6}{2(4-k)}}$, $p_3 \propto t^{-\frac{k+2}{4-k}}$ and $N_e \propto t$. Electrons are accelerated and described by a PL distribution ($\propto \gamma_e^{-p} d\gamma_e$ with $p > 2$), and the magnetic field is magnified in the RS zone. The terms γ_e and p are the Lorentz factor of the electrons and the spectral index, respectively. We consider that a fraction $\varepsilon_{e,r}$ and $\varepsilon_{B,r}$ of the total energy goes to the electrons and the magnetic field, respectively. Therefore, the magnetic field, the minimum and cooling electron Lorentz factors evolve as $B'_r \propto t^{-\frac{k+2}{2(4-k)}}$, $\gamma_{m,r} \propto t^{\frac{2-k}{2(4-k)}}$ and $\gamma_{c,r} \propto t^{\frac{3k-2}{2(4-k)}}$, respectively. Moreover, the synchrotron spectral breaks and the maximum synchrotron flux in terms of observed time are $\nu_{m,r}^{\text{syn}} \propto t^{-\frac{k}{4-k}}$ and $\nu_{c,r}^{\text{syn}} \propto t^{\frac{3k-4}{4-k}}$ and $F_{\text{max},r}^{\text{syn}} \propto t^{\frac{2-k}{4-k}}$, respectively.

Once the RS crosses the shell, the scale of the hydrodynamic variables becomes $\gamma_3 \propto t^{\frac{2k-7}{4(4-k)}}$, $n_3 \propto t^{\frac{2k-13}{4(4-k)}}$, $p_3 \propto t^{\frac{2k-13}{3(4-k)}}$, and $N_e \propto t^0$. In this case, the magnetic field, the minimum and cooling electron Lorentz factors, the synchrotron spectral breaks and the maximum synchrotron flux in terms of the observed time are $B' \propto t^{\frac{2k-13}{6(4-k)}}$, $\gamma_{m,r} \propto t^{\frac{2k-13}{12(4-k)}}$ and $\gamma_{c,r} \propto t^{\frac{25-2k}{12(4-k)}}$, $\nu_{m,r}^{\text{syn}} \propto t^{-\frac{73-14k}{12(4-k)}}$ and $\nu_{c,r}^{\text{syn}} \propto t^{\frac{1+2k}{4(4-k)}}$ and $F_{\text{max},r}^{\text{syn}} \propto t^{-\frac{47-10k}{12(4-k)}}$, respectively. We derive the expected light curves before and after the shock crossing time.

2.1.1 SSC light curves for $t < t_x$

At the deceleration radius $r = 4c(1+z)^{-1}\gamma_3^2 t$, the same electron population can up-scatter synchrotron photons up to higher energies as $h\nu_{i,r}^{\text{SSC}} \sim \gamma_{i,r}^2 h\nu_{i,r}^{\text{syn}}$ with $i = m$ and c , reaching a maximum flux of $F_{\text{max},r}^{\text{SSC}} \sim \frac{4\sigma_T nr}{3g(p)} F_{\text{max},r}^{\text{syn}}$ with $g(p) = \frac{p-1}{p-2}$ ³. Therefore, the SSC spectral breaks and the maximum SSC flux are

$$\begin{aligned} h\nu_{m,r}^{\text{SSC}} &\approx 0.6 \text{ GeV} \left(\frac{1+z}{2}\right)^{\frac{3(k-2)}{4-k}} g^4(2.2) \zeta_{e,-1}^{-4} \varepsilon_{e,r,-1}^4 \varepsilon_{B,r,-2}^{\frac{1}{2}} \Gamma_{2.5}^4 A_{k,-1}^{\frac{3}{4-k}} \Delta_{11.8}^{\frac{k+2}{2(4-k)}} E_{53}^{-\frac{k+2}{2(4-k)}} t_1^{\frac{2(1-k)}{4-k}}, \\ h\nu_{c,r}^{\text{SSC}} &\approx 0.7 \text{ eV} \left(\frac{1+z}{2}\right)^{\frac{2-5k}{4-k}} \left(\frac{1+Y_r}{2}\right)^{-4} \varepsilon_{B,r,-2}^{-\frac{7}{2}} A_{k,-1}^{-\frac{9}{4-k}} \Delta_{11.8}^{\frac{10-7k}{2(4-k)}} E_{53}^{\frac{7k-10}{2(4-k)}} t_1^{\frac{6(k-1)}{4-k}}, \\ F_{\text{max},r}^{\text{SSC}} &\approx 6.8 \text{ mJy} \left(\frac{1+z}{2}\right)^{\frac{2k}{4-k}} g^{-1}(2.2) \zeta_{e,-1} \varepsilon_{B,r,-2}^{\frac{1}{2}} A_{k,-1}^{\frac{4}{4-k}} d_{z,28.3}^{-2} \Gamma_{2.5}^{-1} \Delta_{11.8}^{\frac{12-5k}{2(k-4)}} E_{53}^{\frac{12-5k}{2(4-k)}} t_1^{\frac{4-3k}{4-k}}, \end{aligned} \quad (2)$$

where ζ_e is the fraction of electrons accelerated during the shock (Fan & Piran 2006), Y_r is the Compton parameter and $d_z = (1+z) \frac{c}{H_0} \int_0^z \frac{d\tilde{z}}{\sqrt{\Omega_M(1+\tilde{z})^3 + \Omega_\Lambda}}$ (Weinberg 1972) corresponds to the luminosity distance, with the constant values of $\Omega_M = 1 - \Omega_\Lambda = 0.315$ and $H_0 = 67.4 \text{ km s}^{-1} \text{ Mpc}^{-1}$ (Planck Collaboration et al. 2020). We report the proportionality constants of the spectral breaks and maximum fluxes considering the values of $p = 2.2$ and $t_x = 15 \text{ s}$, unless otherwise stated. At a particular observed energy ($h\nu$), the SSC light curves for the fast- and the slow-cooling regime evolve as

$$F_{\nu,r}^{\text{SSC}}(t < t_x) \propto \begin{cases} t^{-\frac{5k-6}{4-k}} \nu^{\frac{1}{3}}, & \nu < \nu_{c,r}^{\text{SSC}}, \\ t^{\frac{1}{4-k}} \nu^{-\frac{1}{2}}, & \nu_{c,r}^{\text{SSC}} < \nu < \nu_{m,r}^{\text{SSC}}, \\ t^{\frac{(1-k)p+k}{4-k}} \nu^{-\frac{p}{2}}, & \nu_{m,r}^{\text{SSC}} < \nu < \nu_{\text{KN},m,r}^{\text{SSC}}, \end{cases} \quad (3)$$

and

$$F_{\nu,r}^{\text{SSC}}(t < t_x) \propto \begin{cases} t^{-\frac{7k-10}{3(4-k)}} \nu^{\frac{1}{3}}, & \nu < \nu_{m,r}^{\text{SSC}}, \\ t^{\frac{p(1-k)+3-2k}{4-k}} \nu^{-\frac{p-1}{2}}, & \nu_{m,r}^{\text{SSC}} < \nu < \nu_{c,r}^{\text{SSC}}, \\ t^{\frac{(1-k)p+k}{4-k}} \nu^{-\frac{p}{2}}, & \nu_{c,r}^{\text{SSC}} < \nu < \nu_{\text{KN},c,r}^{\text{SSC}}, \end{cases} \quad (4)$$

respectively. Furthermore, the Klein-Nishina (KN) break must be considered since the SSC flux is strongly attenuated if the photon energy lies above this break. For $\nu_{c,r}^{\text{SSC}} < \nu_{m,r}^{\text{SSC}}$ and $\nu_{m,r}^{\text{SSC}} < \nu_{c,r}^{\text{SSC}}$, the KN breaks ($h\nu_{\text{KN},m,r}^{\text{SSC}} \approx \frac{\gamma_3 \gamma_{m,r}}{(1+z)} m_e c^2$ and $h\nu_{\text{KN},c,r}^{\text{SSC}} \approx \frac{\gamma_3 \gamma_{c,r}}{(1+z)} m_e c^2$) become

$$\begin{aligned} h\nu_{\text{KN},m,r}^{\text{SSC}} &\approx 3.7 \times 10 \text{ GeV} \left(\frac{1+z}{2}\right)^{-1} g(2.2) \zeta_{e,-1}^{-1} \varepsilon_{e,r,-1} \Gamma_{2.5}, \\ h\nu_{\text{KN},c,r}^{\text{SSC}} &\approx 0.2 \text{ GeV} \left(\frac{1+z}{2}\right)^{-\frac{k+2}{4-k}} \left(\frac{1+Y_r}{2}\right)^{-1} \varepsilon_{B,r,-2}^{-1} A_{k,-1}^{-\frac{3}{4-k}} \Delta_{11.8}^{\frac{1-k}{4-k}} E_{53}^{\frac{k-1}{4-k}} t_1^{\frac{2(k-1)}{4-k}}, \end{aligned} \quad (5)$$

with m_e the electron mass. Following Nakar et al. (2009) with the definition of a new spectral break ($h\nu_{\text{KN},0,r}^{\text{SSC}} \approx \frac{\gamma_3 \gamma_{0,r}}{(1+z)} m_e c^2$)⁴ the additional PLs in the SSC light curves due to KN effects are

$$F_{\nu,r}^{\text{SSC}}(t < t_x) \propto \begin{cases} t^{\frac{p-k(p-1)}{4-k}} \nu^{-(p-1)}, & \nu_{\text{KN},m,r}^{\text{SSC}} < \nu < \nu_{0,r}^{\text{SSC}}, \\ t^{\frac{p-k(p-1)}{4-k}} \nu^{-(p-\frac{1}{2})}, & \nu_{0,r}^{\text{SSC}} < \nu < \nu_{\text{KN},c,r}^{\text{SSC}}, \\ t^{-\frac{5-3p-k(8-3p)}{3(4-k)}} \nu^{-(p+\frac{1}{3})}, & \nu_{\text{KN},c,r}^{\text{SSC}} < \nu, \end{cases} \quad (6)$$

³ The term σ_T is the Thompson cross-section and h is the Planck constant.

⁴ See eqs. 20 and 49 of Nakar et al. (2009) for the definition of $\gamma_{0,r}$ in the fast ($\gamma_{m,r} > \gamma_{c,r}$) and slow ($\gamma_{c,r} > \gamma_{m,r}$) cooling regimes, respectively.

and

$$F_{\nu,r}^{\text{SSC}}(t < t_x) \propto \begin{cases} t^{\frac{2-k}{4-k}} \nu^{-(p-1)}, & \nu_{\text{KN},c,r}^{\text{SSC}} < \nu < \nu_{0,r}^{\text{SSC}}, \\ t^{\frac{1}{4-k}} \nu^{-\frac{p+1}{2}}, & \nu_{0,r}^{\text{SSC}} < \nu < \nu_{m,r}^{\text{SSC}}, \\ t^{\frac{1}{4-k}} \nu^{-(p+\frac{1}{3})}, & \nu_{m,r}^{\text{SSC}} < \nu, \end{cases} \quad (7)$$

for the fast (weak) - and slow-cooling regimes, respectively.

2.1.2 SSC light curves for $t > t_x$

The SSC spectral breaks and the maximum SSC flux are given by

$$\begin{aligned} h\nu_{m,r}^{\text{SSC}} &\approx 2.7 \times 10^{-3} \text{ eV} \left(\frac{1+z}{2} \right)^{\frac{17-2k}{4(4-k)}} g^4 (2.2) \zeta_{e,-1}^{-4} \varepsilon_{e,-1}^4 \varepsilon_{\text{Br},-2}^{\frac{1}{2}} A_{k,-1}^{-\frac{3}{k-4}} \Gamma_{2.5}^4 \Delta_{11.8}^{\frac{3(4k-15)}{4(k-4)}} E_{53}^{\frac{k+2}{2(k-4)}} t_2^{\frac{3(11-2k)}{4(k-4)}}, \\ h\nu_{\text{cut},r}^{\text{SSC}} &\approx 1.3 \text{ eV} \left(\frac{1+z}{2} \right)^{\frac{17-2k}{4(4-k)}} \varepsilon_{\text{Br},-2}^{-\frac{7}{2}} A_{k,-1}^{\frac{9}{k-4}} \left(\frac{1+Y_r}{2} \right)^{-4} \Delta_{11.8}^{\frac{29+4k}{4(4-k)}} E_{53}^{\frac{10-7k}{2(k-4)}} t_2^{\frac{3(11-2k)}{4(k-4)}}, \\ F_{\text{max},r}^{\text{SSC}} &\approx 0.3 \text{ mJy} \left(\frac{1+z}{2} \right)^{\frac{89-16k}{12(4-k)}} g^{-1} (2.2) \zeta_e \varepsilon_{\text{Br},-2}^{\frac{1}{2}} \Gamma_{2.5}^{-1} A_{k,-1}^{\frac{4}{4-k}} \Delta_{11.8}^{\frac{17-10k}{12(4-k)}} d_{z,28.3}^{-2} E_{53}^{\frac{12-5k}{2(4-k)}} t_2^{\frac{41-4k}{12(k-4)}}, \end{aligned} \quad (8)$$

where the cutoff frequency $\nu_{\text{cut},r}^{\text{SSC}} = \nu_{c,r}^{\text{SSC}}(t_x) \left(\frac{t}{t_x} \right)^{\frac{33-6k}{4(k-4)}}$ is estimated by the requirement that no electrons are shocked anymore and the fluid expands adiabatically. For $\nu_{c,r}^{\text{SSC}} < \nu_{m,r}^{\text{SSC}}$ and $\nu_{m,r}^{\text{SSC}} < \nu_{c,r}^{\text{SSC}}$, the spectral breaks in the KN regime are

$$\begin{aligned} h\nu_{\text{KN},m,r}^{\text{SSC}} &\approx 8.9 \text{ GeV} \left(\frac{1+z}{2} \right)^{-\frac{7-2k}{6(4-k)}} g (2.2) \zeta_{e,-1}^{-1} \varepsilon_{e,-1} \Gamma_{2.5} \Delta_{11.8}^{\frac{17-4k}{6(4-k)}} t_2^{-\frac{17-4k}{6(4-k)}}, \\ h\nu_{\text{KN},c,r}^{\text{SSC}} &\approx 0.8 \text{ GeV} \left(\frac{1+z}{2} \right)^{\frac{13-2k}{3(k-4)}} \left(\frac{1+Y_r}{2} \right)^{-1} \varepsilon_{\text{Br},-2}^{-1} A_{k,-1}^{\frac{3}{k-4}} E_{53}^{\frac{k-1}{4-k}} \Delta_{11.8}^{\frac{2(k-2)}{3(4-k)}} t_2^{\frac{k+1}{3(4-k)}}. \end{aligned} \quad (9)$$

The SSC light curves for the slow-cooling regime evolve as

$$F_{\nu,r}^{\text{SSC}}(t > t_x) \propto \begin{cases} t^{\frac{k+4}{6(k-4)}} \nu^{\frac{1}{3}}, & \nu < \nu_{m,r}^{\text{SSC}}, \\ t^{\frac{17-10k-99p+18kp}{24(4-k)}} \nu^{-\frac{p-1}{2}}, & \nu_{m,r}^{\text{SSC}} < \nu < \nu_{\text{cut},r}^{\text{SSC}}, \\ 0, & \nu_{\text{cut},r}^{\text{SSC}} < \nu. \end{cases}$$

The SSC emission generated in the RS region could decay faster because of the angular time delay effect (Panaitescu & Kumar 2000; Kobayashi & Zhang 2003). During this phase, the evolution of the SSC flux due to high-latitude afterglow emission is described by $F_{\nu,r}^{\text{SSC}}(t > t_x) \propto t^{-(\beta+2)}$, where β is the spectral index with $\beta = 1/2$, $(p-1)/2$ or $p/2$ for the fast and slow cooling regimes, respectively.

2.2 Dynamics of the thin-shell scenario

In the thin-shell regime, the RS becomes mildly relativistic and hence cannot decelerate the shell. In this case, the shock crossing time is longer than the duration of the burst ($T_{90} < t_x$) with $t_x = \left(\frac{(3-k)E(1+z)^{3-k}}{24-k c^5 \pi m_p A_k} \right)^{\frac{1}{3-k}} \Gamma^{-\frac{8-2k}{3-k}}$. Before the RS crosses the shell, the scaling of the hydrodynamic quantities as a function of the observed time is $\gamma_3 \propto t^0$, $n_3 \propto t^{-3}$, $p_3 \propto t^{-k}$, and $N_e \propto t^{\frac{3-k}{2}}$. In this regime, the magnetic field, the minimum, and the cooling electron Lorentz factors evolve as $B'_r \propto t^{-\frac{k}{2}}$, $\gamma_{m,r} \propto t^{-(k-3)}$ and $\gamma_{c,r} \propto t^{k-1}$, respectively. Moreover, the synchrotron spectral breaks and the maximum synchrotron flux in terms of the observed time are $\nu_{m,r}^{\text{syn}} \propto t^{\frac{12-5k}{2}}$ and $\nu_{c,r}^{\text{syn}} \propto t^{\frac{3k-4}{2}}$ and $F_{\text{max},r}^{\text{syn}} \propto t^{\frac{3-2k}{2}}$, respectively.

Once the RS crosses the shell, for $k = 2$, the scaling of the hydrodynamic variables becomes $\gamma_3 \propto t^{-\frac{1}{3}}$, $n_3 \propto t^{-\frac{8}{7}}$, $p_3 \propto t^{-\frac{32}{21}}$ and $N_e \propto t^0$. In this case, the magnetic field, the minimum and cooling electron Lorentz factors, the synchrotron spectral breaks and the maximum synchrotron flux as function of the observed time are $B' \propto t^{-\frac{16}{21}}$, $\gamma_{m,r} \propto t^{-\frac{8}{21}}$ and $\gamma_{c,r} \propto t^{\frac{6}{7}}$, $\nu_{m,r}^{\text{syn}} \propto t^{-\frac{13}{7}}$ and $\nu_{c,r}^{\text{syn}} \propto t^{\frac{13}{21}}$ and $F_{\text{max},r}^{\text{syn}} \propto t^{-\frac{23}{21}}$, respectively. We derive the expected light curves before and after the shock crossing time.

2.2.1 SSC light curves for $t < t_x$

For this time interval, the SSC spectral breaks and the maximum SSC flux are

$$\begin{aligned} h\nu_{m,r}^{\text{SSC}} &\approx 0.2 \text{ eV} \left(\frac{1+z}{2} \right)^{\frac{9k-26}{2}} g^4 (2.2) \zeta_{e,-1}^{-4} \varepsilon_{e,-1}^4 \varepsilon_{\text{Br},-2}^{\frac{1}{2}} A_{k,-1}^{\frac{9}{2}} \Gamma_{1.5}^{34-9k} E_{52}^{-4} t_{2.5}^{\frac{24-9k}{2}}, \\ h\nu_{\text{cut},r}^{\text{SSC}} &\approx 2.7 \times 10^{-6} \text{ eV} \left(\frac{1+z}{2} \right)^{\frac{6-7k}{2}} \varepsilon_{\text{Br},-2}^{-\frac{7}{2}} A_{k,-1}^{-\frac{7}{2}} \left(\frac{1+Y_r}{2} \right)^{-4} \Gamma_{1.5}^{7k-10} t_{2.5}^{\frac{7k-8}{2}}, \\ F_{\text{max},r}^{\text{SSC}} &\approx 0.2 \text{ mJy} \left(\frac{1+z}{2} \right)^{\frac{4k-3}{2}} g^{-1} (2.2) \zeta_{e,-1} \varepsilon_{\text{Br},-2}^{\frac{1}{2}} \Gamma_{1.5}^{7-4k} A_{k,-1}^2 d_{z,28.3}^{-2} E_{52}^{\frac{1}{2}} t_{2.5}^{\frac{5-4k}{2}}. \end{aligned} \quad (10)$$

In analogy to the description of the SSC light curves for the thick-shell regime, the SSC light curves before the shock-crossing time for the fast- and the slow-cooling regimes at a particular observed energy are

$$F_{\nu,r}^{\text{SSC}}(t < t_x) \propto \begin{cases} t^{\frac{23-19k}{6}} \nu^{\frac{1}{3}}, & \nu < \nu_{c,r}^{\text{SSC}}, \\ t^{\frac{2-k}{4}} \nu^{-\frac{1}{2}}, & \nu_{c,r}^{\text{SSC}} < \nu < \nu_{m,r}^{\text{SSC}}, \\ t^{\frac{3p(8-3k)+2(4k-11)}{4}} \nu^{-\frac{p}{2}}, & \nu_{m,r}^{\text{SSC}} < \nu < \nu_{\text{KN},m,r}^{\text{SSC}}, \end{cases} \quad (11)$$

and

$$F_{\nu,r}^{\text{SSC}}(t < t_x) \propto \begin{cases} t^{-\frac{k+3}{2}} \nu^{\frac{1}{3}}, & \nu < \nu_{c,r}^{\text{SSC}}, \\ t^{\frac{3p(8-3k)+k-14}{4}} \nu^{-\frac{p-1}{2}}, & \nu_{m,r}^{\text{SSC}} < \nu < \nu_{c,r}^{\text{SSC}}, \\ t^{\frac{3p(8-3k)+2(4k-11)}{4}} \nu^{-\frac{p}{2}}, & \nu_{c,r}^{\text{SSC}} < \nu < \nu_{\text{KN},c,r}^{\text{SSC}}, \end{cases} \quad (12)$$

respectively. For $\nu_{c,r}^{\text{SSC}} < \nu_{m,r}^{\text{SSC}}$ and $\nu_{m,r}^{\text{SSC}} < \nu_{c,r}^{\text{SSC}}$, the spectral breaks in the KN regime are

$$\begin{aligned} h\nu_{\text{KN},m,r}^{\text{SSC}} &\approx 6.1 \times 10^{-2} \text{ GeV} \left(\frac{1+z}{2}\right)^{k-4} g(2.2) \zeta_{e,-1}^{-1} \varepsilon_{e,-1} A_{k,-1} \Gamma_{1.5}^{9-2k} E_{52}^{-1} t_{2.5}^{3-k}, \\ h\nu_{\text{KN},c,r}^{\text{SSC}} &\approx 3.9 \times 10^{-3} \text{ GeV} \left(\frac{1+z}{2}\right)^{-k} \left(\frac{1+Y_r}{2}\right)^{-1} \varepsilon_{\text{Br},-2}^{-1} A_{k,-1}^{-1} \Gamma_{1.5}^{2(k-1)} t_{2.5}^{k-1}. \end{aligned} \quad (13)$$

In analogy to the description of the SSC light curves for the thick-shell regime, the additional PLs in the SSC light curves due to KN effects are (Nakar et al. 2009)

$$F_{\nu,r}^{\text{SSC}}(t < t_x) \propto \begin{cases} t^{-\frac{2(17-15p)-k(12-11p)}{4}} \nu^{-(p-1)}, & \nu_{\text{KN},m,r}^{\text{SSC}} < \nu < \nu_{0,r}^{\text{SSC}}, \\ t^{-\frac{2(14-15p)-k(10-11p)}{4}} \nu^{-(p-\frac{1}{2})}, & \nu_{0,r}^{\text{SSC}} < \nu < \nu_{\text{KN},c,r}^{\text{SSC}}, \\ t^{-\frac{2(47-45p)-k(40-33p)}{12}} \nu^{-(p+\frac{1}{3})}, & \nu_{\text{KN},c,r}^{\text{SSC}} < \nu, \end{cases} \quad (14)$$

and

$$F_{\nu,r}^{\text{SSC}}(t < t_x) \propto \begin{cases} t^{-\frac{2(9-11p)-k(4-7p)}{4}} \nu^{-(p-1)}, & \nu_{\text{KN},c,r}^{\text{SSC}} < \nu < \nu_{0,r}^{\text{SSC}}, \\ t^{-\frac{8(1-2p)-k(2-5p)}{4}} \nu^{-\frac{p+1}{2}}, & \nu_{0,r}^{\text{SSC}} < \nu < \nu_{m,r}^{\text{SSC}}, \\ t^{-\frac{6(5-11p)-k(8-21p)}{12}} \nu^{-(p+\frac{1}{3})}, & \nu_{m,r}^{\text{SSC}} < \nu, \end{cases} \quad (15)$$

for the fast (weak) - and slow-cooling regimes, respectively.

2.2.2 SSC light curves for $t > t_x$ with $k = 2$

Following the previous process, the spectral breaks and the maximum flux of SSC emission are given by

$$\begin{aligned} h\nu_{m,r}^{\text{SSC}} &\approx 0.7 \text{ eV} \left(\frac{1+z}{2}\right)^{\frac{34}{21}} g^4(2.2) \zeta_{e,-1}^{-4} \varepsilon_{e,-1}^4 \varepsilon_{\text{Br},-2}^{\frac{1}{2}} A_{k,-1}^{-\frac{47}{42}} \Gamma_{1.5}^{-\frac{136}{21}} E_{52}^{\frac{34}{21}} t_{3.5}^{-\frac{55}{21}}, \\ h\nu_{\text{cut},r}^{\text{SSC}} &\approx 1.0 \times 10^{-4} \text{ eV} \left(\frac{1+z}{2}\right)^{\frac{34}{21}} \left(\frac{1+Y_r}{2}\right)^{-4} \varepsilon_{\text{Br},-2}^{-\frac{7}{2}} A_{k,-1}^{-\frac{383}{42}} \Gamma_{1.5}^{-\frac{388}{21}} E_{52}^{\frac{118}{21}} t_{3.5}^{-\frac{55}{21}}, \\ F_{\text{max},r}^{\text{SSC}} &\approx 4.9 \times 10^{-3} \text{ mJy} \left(\frac{1+z}{2}\right)^{\frac{17}{7}} g^{-1}(2.2) \zeta_{e,-1}^{\frac{1}{2}} \varepsilon_{\text{Br},-2}^{\frac{1}{2}} A_{k,-1}^{\frac{29}{14}} \Gamma_{1.5}^{-\frac{5}{7}} d_{z,28.3}^{-2} E_{52}^{\frac{3}{7}} t_{3.5}^{-\frac{10}{7}}, \end{aligned} \quad (16)$$

where the cutoff frequency $\nu_{\text{cut},r}^{\text{SSC}} = \nu_{c,r}^{\text{SSC}}(t_x) \left(\frac{t}{t_x}\right)^{-\frac{55}{21}}$ is estimated by the requirement that no electrons are shocked anymore and the fluid expands adiabatically. For $\nu_{c,r}^{\text{SSC}} < \nu_{m,r}^{\text{SSC}}$ and $\nu_{m,r}^{\text{SSC}} < \nu_{c,r}^{\text{SSC}}$, the spectral breaks in the KN regime are given by

$$\begin{aligned} h\nu_{\text{KN},m,r}^{\text{SSC}} &\approx 0.1 \text{ GeV} \left(\frac{1+z}{2}\right)^{-\frac{2}{7}} g(2.2) \zeta_{e,-1}^{-1} \varepsilon_{e,-1} A_{k,-1}^{-\frac{5}{7}} \Gamma_{1.5}^{-\frac{13}{7}} E_{52}^{\frac{5}{7}} t_{3.5}^{-\frac{5}{7}}, \\ h\nu_{\text{KN},c,r}^{\text{SSC}} &\approx 2.4 \times 10^{-2} \text{ GeV} \left(\frac{1+z}{2}\right)^{-\frac{32}{21}} \left(\frac{1+Y_r}{2}\right)^{-1} \varepsilon_{\text{Br},-2}^{-1} A_{k,-1}^{-\frac{31}{21}} \Gamma_{1.5}^{\frac{2}{21}} E_{52}^{\frac{10}{21}} t_{3.5}^{\frac{11}{21}}. \end{aligned} \quad (17)$$

The SSC light curves for the slow-cooling regime are

$$F_{\nu,r}^{\text{SSC}}(t > t_x) \propto \begin{cases} t^{-\frac{5}{9}} \nu^{\frac{1}{3}}, & \nu < \nu_{c,r}^{\text{SSC}}, \\ t^{-\frac{5(11p+1)}{42}} \nu^{-\frac{p-1}{2}}, & \nu_{m,r}^{\text{SSC}} < \nu < \nu_{\text{cut},r}^{\text{SSC}}, \\ 0, & \nu_{\text{cut},r}^{\text{SSC}} < \nu. \end{cases}$$

The SSC emission from the RS region could decay faster due to the angular time delay effect. During the emission at high latitudes, the SSC flux evolves in the same manner as the flux mentioned above in the case of the thick-shell scenario.

2.3 Synchrotron light curves from forward shocks

The dynamics of the forward shocks for a relativistic outflow expanding into a constant-density ($k = 0$) and stellar-wind environments ($k = 2$) are treated in Sari et al. (1998); Chevalier & Li (2000); Panaitescu & Kumar (2000). For a density profile $\propto r^{-k}$, the evolution of the bulk

Lorentz factor is $\Gamma \propto t^{-\frac{3-k}{2(4-k)}}$, and the electron Lorentz factors for the minimum and the cooling energy are $\gamma_{m,f} \propto t^{-\frac{3-k}{2(4-k)}}$ and $\gamma_{c,f} \propto t^{\frac{k+1}{2(4-k)}}$, respectively. Using the evolution of synchrotron energy breaks ($\nu_{m,f}^{\text{syn}} \propto t^{-\frac{3}{2}}$ and $\nu_{c,f}^{\text{syn}} \propto t^{\frac{4-3k}{2(k-4)}}$) and the maximum flux ($F_{\text{max},f}^{\text{syn}} \propto t^{\frac{k}{2(k-4)}}$), the observed flux in the fast cooling regime is proportional to $F_{\nu,f}^{\text{syn}} \propto t^{-\frac{1}{4}} \nu^{-\frac{1}{2}}$ for $\nu < \nu_{m,f}^{\text{syn}}$ and $\propto t^{-\frac{3p-2}{4}} \nu^{-\frac{p}{2}}$ for $\nu_{m,f}^{\text{syn}} < \nu$. In the slow cooling regime, the observed flux is proportional to $F_{\nu,f}^{\text{syn}} \propto t^{\frac{12-5k-3p(4-k)}{4(4-k)}} \nu^{-\frac{p-1}{2}}$ for $\nu < \nu_{c,f}^{\text{syn}}$ and $\propto t^{-\frac{3p-2}{4}} \nu^{-\frac{p}{2}}$ for $\nu_{c,f}^{\text{syn}} < \nu$.

2.4 The Compton Y-parameter

When KN effects are strong, the Compton parameter changes. In this case, this parameter in the slow-cooling regime can be estimated with

$$Y_j(Y_j + 1) = Y_{0,j} \begin{cases} 1 & \text{for } \nu_{c,j}^{\text{syn}} < \nu_{\text{KN},c,j}^{\text{syn}} \\ \left(\frac{\nu_{\text{KN},c,j}^{\text{syn}}}{\nu_{c,j}^{\text{syn}}} \right)^{-\frac{p-3}{2}} & \text{for } \nu_{m,j}^{\text{syn}} < \nu_{\text{KN},c,j}^{\text{syn}} < \nu_{c,j}^{\text{syn}} \\ \left(\frac{\nu_{m,j}^{\text{syn}}}{\nu_{c,j}^{\text{syn}}} \right)^{-\frac{p-3}{2}} \left(\frac{\nu_{\text{KN},c,j}^{\text{syn}}}{\nu_{m,j}^{\text{syn}}} \right)^{\frac{4}{3}} & \text{for } \nu_{\text{KN},c,j}^{\text{syn}} < \nu_{m,j}^{\text{syn}}, \end{cases} \quad (18)$$

where $Y_{0,j} = \frac{\epsilon_{e,j}}{\epsilon_{B,j}} \left(\frac{\gamma_{m,j}}{\gamma_{c,j}} \right)^{p-2}$ with $j = r$ or f . For the RS region, $h\nu_{\text{KN},c,r}^{\text{syn}} \simeq \frac{\gamma_3}{(1+z)} \frac{m_e c^2}{\gamma_{c,r}}$ for $\nu_{c,r}^{\text{syn}} > \nu_{m,r}^{\text{syn}}$ (see Nakar et al. 2009; Wang et al. 2010). It is worth mentioning that in the fast cooling regime the synchrotron break in the KN regime becomes $h\nu_{\text{KN},m,r}^{\text{syn}} \simeq \frac{\gamma_3}{(1+z)} \frac{m_e c^2}{\gamma_{m,r}}$ for $\nu_{c,r}^{\text{syn}} < \nu_{m,r}^{\text{syn}}$. For the FS region, $h\nu_{\text{KN},c,f}^{\text{syn}} \simeq \frac{\Gamma}{(1+z)} \frac{m_e c^2}{\gamma_{c,f}}$ for $\nu_{c,f}^{\text{syn}} > \nu_{m,f}^{\text{syn}}$ and $h\nu_{\text{KN},m,f}^{\text{syn}} \simeq \frac{\gamma_3}{(1+z)} \frac{m_e c^2}{\gamma_{m,f}}$ for $\nu_{c,f}^{\text{syn}} < \nu_{m,f}^{\text{syn}}$. To describe the LAT data above 100 MeV, we must determine the Lorentz factor of electrons that may produce high-energy photons via the synchrotron process, include a new spectrum break, and recalculate the Compton value. The new spectral break becomes $h\nu_{\text{KN},c,j}^{\text{syn}}(\gamma_*)$, and the recalculated Compton parameter, $Y(\gamma_*)$, becomes $Y(\gamma_*) = Y(\gamma_{c,j}) \left(\frac{\nu_*}{\nu_{c,j}} \right)^{\frac{p-3}{4}} \left(\frac{\nu_{\text{KN},c,j}^{\text{syn}}(\gamma_{c,j})}{\nu_{c,j}^{\text{syn}}} \right)^{-\frac{p-3}{2}}$ for $\nu_{m,j}^{\text{syn}} < h\nu_{\text{KN},c,j}^{\text{syn}}(\gamma_*) = 100 \text{ MeV} < \nu_{c,j}^{\text{syn}} < \nu_{\text{KN},c,j}^{\text{syn}}(\gamma_{c,j})$ (for details, see Wang et al. 2010).

2.5 The maximum photon energy

2.5.1 Reverse-shock region

The maximum energy radiated by the SSC process can be estimated by equalising the acceleration ($\propto \gamma_e B_r'^{-1}$) and the synchrotron ($\propto \gamma_e^{-1} B_r'^{-2}$) timescales. The maximum Lorentz factor of the electron distribution is $\gamma_{\text{max},r} = (3q_e/\xi\sigma_T B_r')^{\frac{1}{2}}$ with ξ the Bohm parameter⁵ and q_e the elementary charge. Therefore, the maximum energy radiated by the synchrotron model is $h\nu_{\text{max},r}^{\text{syn}} = 3q_e^2 \gamma_3 / 2\pi\sigma_T m_e c (1+z)$. In this case, the maximum energy generated by the SSC mechanism for $t < t_x$ in the thick and thin regime is

$$h\nu_{\text{max},r}^{\text{SSC}} \simeq 1.3 \text{ GeV} \left(\frac{1+z}{2} \right)^{-\frac{4}{4-k}} \epsilon_{\text{Br},-2}^{-\frac{1}{2}} A_{k,-1}^{-\frac{2}{4-k}} \Delta_{11.8}^{-\frac{k}{2(4-k)}} E_{53}^{\frac{k}{2(4-k)}} t_1^{\frac{k}{4-k}}, \quad (19)$$

and

$$h\nu_{\text{max},r}^{\text{SSC}} \simeq 0.4 \text{ GeV} \left(\frac{1+z}{2} \right)^{-\frac{k+2}{2}} \epsilon_{\text{Br},-2}^{-\frac{1}{2}} A_{k,-1}^{-\frac{1}{2}} \Gamma_{1.5}^k t_{2.5}^{\frac{k}{2}}, \quad (20)$$

respectively. For $t > t_x$, the maximum energies are determined by $\nu_{\text{cut},r}^{\text{SSC}}$.

2.5.2 Forward-shock region

The maximum Lorentz factor of the electron distribution is $\gamma_{\text{max},f} = (3q_e/\xi\sigma_T B_f')^{\frac{1}{2}}$ and the maximum energy radiated by the synchrotron yields

$$h\nu_{\text{max},f}^{\text{syn}} \simeq 0.2 \text{ GeV} \left(\frac{1+z}{2} \right)^{\frac{k-5}{2(4-k)}} A_{k,-1}^{-\frac{1}{2(4-k)}} E_{53}^{\frac{1}{2(4-k)}} t_2^{-\frac{3-k}{2(4-k)}}. \quad (21)$$

⁵ In the Bohm limit, this parameter becomes $\xi \sim 1$.

2.6 The short-lasting bright peak and the long-lasting emission in the *Fermi*/LAT band

We display in Figure 1 the expected SSC and synchrotron light curves from the RS and FS model when the outflow decelerates in a stellar-wind density ($k = 2$). They are presented in the fast and slow cooling regime, and when the RS lies in the thick (left column) and thin (right column) shell case. Possible transitions between the fast- and slow-cooling regimes and from constant-density to stellar-wind medium are not considered. The effects in the self-absorption regime are not considered because they are unimportant at the *Fermi*/LAT energy range (e.g., see Panaitescu et al. 2014). The SSC RS flux in blue lines illustrates that a peak is expected at $t = t_x$ when it evolves in $\nu_{c,r}^{\text{SSC}} < \nu_{\text{LAT}} < \nu_{m,r}^{\text{SSC}}$ for the thick-shell case and $\nu_{c,r}^{\text{SSC}} < \nu_{\text{LAT}} < \nu_{c,r}^{\text{SSC}}$ for the thin-shell case. Otherwise, the flux decreases monotonically, exhibiting a break at $t = t_x$. The temporal break is associated with the transition time (black line). Under the cooling conditions $\nu_{c,r}^{\text{SSC}} < \nu_{\text{LAT}} < \nu_{\text{cut},r}^{\text{SSC}}$ and $t_x < t$, the light curves in the thick and thin regime could exhibit a temporal break due to the passage of the cutoff break through the *Fermi*/LAT band ($\nu_{\text{cut},r}^{\text{SSC}} < \nu_{\text{LAT}}$).

The expected synchrotron FS fluxes in red lines are shown for a stellar-wind medium. Since the spectral breaks evolve as $\nu_{m,f}^{\text{syn}} \propto t^{-\frac{3}{2}}$ and $\nu_{c,f}^{\text{syn}} \propto t^{\frac{1}{2}}$, the temporal breaks displayed in the synchrotron FS fluxes correspond to the transitions from $\nu_{\text{LAT}} < \nu_{m,f}^{\text{syn}}$ to $\nu_{m,f}^{\text{syn}} < \nu_{\text{LAT}}$ for the fast cooling regime, and from $\nu_{c,f}^{\text{syn}} < \nu_{\text{LAT}}$ to $\nu_{\text{LAT}} < \nu_{c,f}^{\text{syn}}$ for the slow cooling regime.

We argue that a LAT light curve with similar features to that shown in Figure 1 can be described as a superposition of SSC RS and synchrotron FS emissions evolving in a stellar wind environment. It is worth noting that, depending on the value of the shock crossing time, the SSC emission would appear during the prompt emission (thick shell) or later (thin shell).

3 APPLICATION: SECOND *FERMI*/LAT CATALOG

3.1 Our sample of GRBs

3.1.1 GRB 080916C

GRB 080916C triggered the Gamma Burst Monitor (GBM) instrument on board the *Fermi* satellite at 00:12:45.613542 UT on September 16, 2008 (Goldstein & van der Horst 2008). The duration of prompt emission measured by the GBM instrument was $T_{90} = 62.98$ s correspondent to a fluence of $(4.0 \pm 0.6) \times 10^{-5}$ erg cm $^{-2}$ and an isotropic energy of $E_{\gamma,\text{iso}} = (1.7 \pm 0.1) \times 10^{54}$ erg (Ajello et al. 2019). This burst was detected at a redshift $z = 4.35 \pm 0.15$ (Clemens et al. 2008) at R.A.=08^h07^m12^s and Dec=-61° 18'00" with a 2.8° uncertainty at 68 percent. In the energy range of 10 keV to 10 GeV, the apparent isotropic energy release was measured as 8.8×10^{54} erg (Abdo et al. 2009a). The *Swift*/XRT instrument began observing GRB 080916C at 17:08 UT, 17 hours after trigger time (Perri et al. 2008). This instrument monitored GRB 080916C in the Photon Counting (PC) mode from 6.1×10^4 to $\sim 10^6$ s. The best-fit intrinsic absorption column density is 1.49×10^{21} cm $^{-2}$. GRB 080916C was detected by the Gamma-Ray Burst Optical/Near-Infrared Detector in optical bands (GROND; Clemens et al. 2008).

3.1.2 GRB 090323

At 00:02:42.63 UT on March 23, 2009, GRB 090323 triggered the *Fermi*/GBM instrument (Ohno et al. 2009). The duration of the prompt emission measured by the GBM instrument was $T_{90} = 133.89$ s, corresponding to a fluence of $(0.26 \pm 0.07) \times 10^{-5}$ erg cm $^{-2}$ and an isotropic energy of $E_{\gamma,\text{iso}} = (3.0 \pm 2.0) \times 10^{53}$ erg (Ajello et al. 2019). The *Fermi*/LAT instrument also detected this burst (Kennea et al. 2009; Perri & Stratta 2009). The isotropic energy in the LAT energy range was $\simeq 4.1 \times 10^{54}$ erg (Ackermann et al. 2013a). The *Swift*/XRT instrument began observing GRB 090323 at 19:27 UT, 19.4 hours after the trigger. This instrument monitored GRB 090323 in the PC mode with a spectrum exposure of 6 ks. The best-fit intrinsic absorption column density is 2.20×10^{22} cm $^{-2}$ with a redshift $z = 3.57$, which was measured by Chornock et al. (2009). McBreen et al. (2010) described the burst's optical and infrared observations in great detail.

3.1.3 GRB 090902B

GRB 090902B was detected by the *Fermi*/GBM instrument on 2009 September 2 at 11:05:08.31 UT with coordinates R.A.= 17^h38^m26^s and Dec: 26° 30'. The duration of the prompt emission in the energy band 50 - 300 keV was $T_{90} = 19.33$ s, corresponding to a fluence $(7.0 \pm 1.0) \times 10^{-5}$ erg cm $^{-2}$, and an isotropic energy of $E_{\gamma,\text{iso}} = (3.7 \pm 0.3) \times 10^{53}$ erg (Ajello et al. 2019). The burst was within the *Fermi*/LAT field of view initially at an angle of 51° from the sight of vision. The X-ray afterglow was detected within the LAT error circle by the *Swift*/XRT (Kennea & Stratta 2009), and Ultraviolet/Optical Telescope (UVOT) (Swenson & Siegel 2009), and later by several other ground-based telescopes. The XRT instrument monitored GRB 090902B in the PC mode with a spectrum exposure of 13.5 ks. The best-fit intrinsic absorption column density is $2.3^{+0.8}_{-0.6} \times 10^{22}$ cm $^{-2}$ with a redshift $z = 1.822$, which was determined by the Gemini-North telescope (Cucchiara et al. 2009).

3.1.4 GRB 090926A

GRB 090926A was discovered by the *Fermi*/GBM at 04:20:26.99 UT on 26 September 2009, with coordinates R.A.=354.5° and Dec=-64.2° (Ackermann et al. 2011). The duration of the prompt emission, fluence and isotropic energy measured by GBM instrument were $T_{90} = 13.76$ s, $(2.9 \pm 0.3) \times 10^{-5}$ erg cm⁻², and $E_{\gamma, \text{iso}} = (5.3 \pm 0.4) \times 10^{53}$ erg, respectively (Ajello et al. 2019). GRB 090926A presented a characteristic high-energy PL component that is different from the known Band function, according to a joint LAT and GBM data analysis (Ackermann et al. 2011). *Swift*/XRT, INTEGRAL SPI-ACS (Bissaldi 2009), Suzaku/WAM (Noda et al. 2009), CORONAS-Photon (Chakrabarti et al. 2009), the Konus-wind experiment (Golenetskii et al. 2009) and the Ultra-violet Optical Telescope (UVOT) instrument on board *Neil Gehrels Swift Observatory* (Malesani et al. 2009), all identified this burst separately. The *Swift*/XRT instrument began observing GRB 090926A, 13.9 hours after the trigger. This instrument monitored GRB 090926A in the PC mode since 4.7×10^4 to 1.8×10^6 s. The best-fit intrinsic absorption column density is $3.0_{-3.0}^{+4.0} \times 10^{21}$ cm⁻² with a redshift $z = 2.1062$, which was estimated using X-shooter installed on the Very Large Telescope (Malesani et al. 2009).

3.1.5 GRB 110731A

GRB 110731A triggered the *Fermi*/GBM instrument at 11:09:29.94 UT on 2011 July 31 (Ackermann et al. 2013b). Approximately 30 s after the GBM trigger, the Burst Alert Telescope (BAT) on board *Neil Gehrels Swift Observatory* was also set off, and it located GRB 110731A at R.A.=18^h42^m05^s and Dec=-28°32'44" with an uncertainty of 3 arcmin. The duration of the prompt emission measured by GBM instrument was $T_{90} = 7.49$ s, corresponding to a fluence and an isotropic energy of $(0.930 \pm 0.07) \times 10^{-5}$ erg cm⁻² and $E_{\gamma, \text{iso}} = (1.2 \pm 0.3) \times 10^{53}$ erg, respectively (Ajello et al. 2019). The isotropic energy measured using a PL and a Band function was $(7.6 \pm 0.2) \times 10^{53}$ erg (Ackermann et al. 2013b). The *Swift*/XRT instrument started detecting GRB 110731A at 11:10:36.9 UT, 66.4 s after the BAT trigger (Oates et al. 2011). This instrument monitored GRB 110731A in the windowed-timing (WT) mode with a spectrum exposure of 573 s and the PC mode with a spectrum exposure of 7.5 ks. The best-fit intrinsic absorption column density is $4.4_{-3.0}^{+3.1} \times 10^{21}$ cm⁻². The Swift UVOT instrument began observing the burst's position 75 s after the BAT trigger (Oates et al. 2011). Following the *Swift*/BAT trigger, several efforts were undertaken to observe the burst's position, such as those by the Faulkes Telescopes North and South (Bersier 2011), the Nordic Optical Telescope equipped with ALFOSC (Malesani et al. 2011), Konus-Wind (Golenetskii et al. 2011), the EVLA (Zauderer et al. 2011), the Suzaku Wide-band All-sky Monitor (WAM) (Hanabata et al. 2011) and the SAO RAS and Terskol observatories (Moskvitin et al. 2011). Tanvir et al. (2011) obtained spectroscopic observations with the GMOS-N instrument on Gemini-North, which led to an estimation of a redshift of $z = 2.83$.

3.1.6 GRB 130427A

GRB 130427A triggered the *Fermi*/GBM instrument at 07:47:06.42 UTC on April 27, 2013 (von Kienlin 2013). Approximately 50 s after the initial trigger, it also triggered the *Swift*/BAT instrument. Following the initial triggers, there was a substantial follow-up campaign by extraterrestrial observatories and ground-based experiments (from the ultra-violet, optical and X-ray telescopes (Maselli et al. 2014); SPI-ACS/INTEGRAL (Pozenenko et al. 2013); AGILE (Verrecchia et al. 2013); Konus-Wind (Golenetskii et al. 2013); NuSTAR (Kouveliotou et al. 2013); RHESSI (Smith et al. 2013); MAXI/GSC (Kawamuro et al. 2013); VLT/X-shooter (Flores et al. 2013)). The duration of the prompt emission measured by GBM instrument was $T_{90} = 138.24$ s (Ajello et al. 2019) with an isotropic energy of $E_{\gamma, \text{iso}} = (1.7 \pm 0.2) \times 10^{52}$ erg (Ajello et al. 2019). The total fluence and the isotropic energy measured in the 10 keV - 100 GeV range was 4.9×10^{-3} erg cm⁻² and 1.4×10^{54} erg, respectively (Ackermann et al. 2014). The *Swift*/XRT instrument started observing GRB 130427A at 07:50:17.7 UT, 140.2 s after the BAT trigger. This instrument monitored GRB 130427A in the WT mode with a spectrum exposure of 1.9 ks and the PC mode with a spectrum exposure of 4.1 ks. The best-fitting absorption column (intrinsic) is $2.7_{-0.8}^{+0.8} \times 10^{20}$ cm⁻² and $1.1_{-0.4}^{+0.4} \times 10^{21}$ cm⁻² for WT and PC modes, respectively. The Combined Array for Research in Millimeter-wave Astronomy (CARMA) localized this burst to R.A. = 173.1367°, Dec. = 27.6989° (J2000) with an uncertainty of 0.4 arc sec (Perley 2013). Optical spectroscopy from Gemini-North conducted by Levan et al. (2013) found the redshift of the GRB to be $z = 0.34$.

3.1.7 GRB 160625B

Fermi/GBM triggered and located GRB 160625B at 22:40:16.28 UT, 2016 June 25 (Burns 2016). Immediately, *Fermi*/LAT triggered this burst at 22:43:24.82 UT (Dirirsa et al. 2016). The duration of the prompt emission measured by the GBM instrument was $T_{90} = 453.38$ s, corresponding to a fluence and an isotropic energy of $(2.5 \pm 0.3) \times 10^{-5}$ erg cm⁻² and $E_{\gamma, \text{iso}} = (1.5 \pm 0.1) \times 10^{53}$ erg, respectively (Ajello et al. 2019). The *Swift*/XRT instrument monitored GRB 160625B in the PC mode from 9.8×10^4 to 4.1×10^6 s. The best-fit absorption column (intrinsic) is $1.6 \pm 0.6 \times 10^{21}$ cm⁻², with a redshift $z = 1.406$ (Xu et al. 2016). Several optical observations were performed with background telescopes (Zhang et al. 2016; Troja et al. 2017).

3.1.8 GRB 180720B

GRB 180720B was identified and immediately followed by GBM and LAT instruments, the two instruments onboard the *Fermi* satellite (Roberts & Meegan 2018; Bissaldi & Racusin 2018), and BAT, XRT, and UVOT instruments onboard the Swift satellite (Palmer et al. 2018; Barthelmy et al. 2018). The BAT instrument triggered this burst on July 20, 2018, at 14:21:44 UT and located it with coordinates: R.A. = 00^h02^m07^s and Dec = -02^d56′00″ (J2000) with an uncertainty of 3 arcmin. The duration of the prompt emission measured by the GBM instrument was $T_{90} = 48.90$ s correspondent to a fluence $(0.19 \pm 0.05) \times 10^{-5}$ erg cm⁻², and an isotropic energy of $E_{\gamma, \text{iso}} = (0.39 \pm 0.09) \times 10^{52}$ erg (Ajello et al. 2019). The *Swift*/XRT instrument started observing GRB 180720B at 14:23:11.0 UT, 86.5 s after the BAT trigger. This instrument monitored GRB 180720B in the WT mode with a spectrum exposure of 2.2 ks and the PC mode with a spectrum exposure of 3.9 ks. The best-fitting absorption column (intrinsic) is $3.72^{+0.11}_{-0.11} \times 10^{21}$ cm⁻² and $3.4^{+0.6}_{-0.5} \times 10^{21}$ cm⁻² for WT and PC modes, respectively. GRB 180720B started to be monitored in the optical and near-infrared (NIR) bands on July 20, 2018, at 14:22:57 UT, 73 s after the trigger time (Sasada et al. 2018). Vreeswijk et al. (2018) detected the optical emission of GRB 180720B using the VLT/X-shooter spectrograph, associating a redshift of $z = 0.654$.

3.2 Data analysis

The data files used for the *Fermi*/LAT analysis were obtained from the online data website.⁶ *Fermi*/LAT data was analyzed in the 0.1-100 GeV energy range and within the time-resolved likelihood analysis for each burst ($t_{\text{LAT},0}$, $t_{\text{LAT},1}$, see Table 1 from Ajello et al. (2019) for the definition) with the *Fermi* Science tools⁷ in their conda-based installation. `ScienceTools 2.2.0`⁸ For this analysis we adopt the responses reported for each burst by Ajello et al. (2019), following the unbinned likelihood analysis presented by the *Fermi*/LAT team.⁹ Using the `gtselect` tool, we select, with an event class 32 nor 8 depending on the response chosen¹⁰, a region of interest (ROI) around the position of the burst within a radius of 15°. We apply a cut to the zenith angle above 100°. Then, we select the appropriate time intervals (GTIs) using the `gtmktime` tool on the selected data before considering the ROI cut. To define the model needed to describe the source, the diffuse components and point sources of 4FGL-DR3 reported by Abdollahi et al. (2022) embedded in ROI `make4FGLxml`¹¹ were used. We define a point source at the position of this burst, assuming a PL spectrum, and we define a diffuse galactic component using GALPROP `gll_iem_v07` as well as the extragalactic background `iso_P8R3_SOURCE_V3_v1`¹². For each burst, the spectral index is fixed with the value reported by Ajello et al. (2019) in their Table 4, letting free the normalisation and the normalisation of the diffuse component. We use `gtdiffrsp` to take into account all of these components. Following the likelihood procedure, we produce a lifetime cube with the tool `gltcube`, using a step $\delta\theta = 0.025$, a bin size of 0.5 and a maximum zenith angle of 100°. The exposure map was created using `gtexpmap`, considering a region of 30° around the GRB position and defining 100 spatial bins in longitude/latitude and 50 energy bins, and we perform the likelihood analysis with `pyLikelihood`¹³. Finally, we obtain the photons with a probability greater than 90% to be associated to each burst with the `gtsrcprob` tool.

The upper panels in each plot of Figure 2 show the *Fermi*/LAT energy flux (blue) and photon flux (red) light curves, and the lower panels exhibit all photons with energies ≥ 100 MeV associated with GRB 080916C, GRB 090323, GRB 090902B, GRB 090926A, GRB 110731A, GRB 130427A, GRB 160625B and GRB 180720B. The filled circles in black correspond to the individual photons and their energies with probability $> 90\%$ of being associated with the respective burst and the open circles in grey indicate the LAT gamma transient class photons.

In order to describe the short-lasting peak in the LAT observations, we use the function

$$F_{L, \text{se}}(t) = A_{\text{se}} \begin{cases} (t - T_a)^{-\alpha_{r, \text{bb}}} & t < t_{r, \text{br}}, \\ t^{-\alpha_{r, \text{ab}}} & t_{r, \text{br}} < t, \end{cases} \quad (22)$$

where A_{se} corresponds to the proportionality constant, $t_{r, \text{br}}$ is the temporal break with the temporal indexes before ($\alpha_{r, \text{bb}}$) and after ($\alpha_{r, \text{ab}}$) the break. The term T_a is the starting time of the short-term component (Kobayashi & Zhang 2007; Vestrand et al. 2006). For the long-lasting component, we use a PL function $F_{L, \text{ee}}(t) = A_{\text{ee}} t^{-\alpha_f}$ or BPL function

$$F_{L, \text{ee}}(t) = A_{\text{ee}} \begin{cases} t^{-\alpha_{f, \text{bb}}} & t < t_{f, \text{br}}, \\ t^{-\alpha_{f, \text{ab}}} & t_{f, \text{br}} < t, \end{cases} \quad (23)$$

where A_{ee} corresponds to the proportionality constant, $t_{f, \text{br}}$ is the temporal break with the temporal indexes before ($\alpha_{f, \text{bb}}$) and after ($\alpha_{f, \text{ab}}$) the break with f = L, X, O for LAT, X-ray and optical observations, respectively. The continuous and dashed lines on the photon energy flux

⁶ <https://fermi.gsfc.nasa.gov/cgi-bin/ssc/LAT/LATDataQuery.cgi>

⁷ <https://fermi.gsfc.nasa.gov/ssc/data/analysis/software/>

⁸ <https://github.com/Fermi/LAT/Fermitools-conda/wiki>

⁹ https://fermi.gsfc.nasa.gov/ssc/data/analysis/scitools/likelihood_tutorial.html

¹⁰ <https://fermi.gsfc.nasa.gov/ssc/data/analysis/documentation/Cicerone/>

[Cicerone_Data/LAT_DP.html](https://fermi.gsfc.nasa.gov/ssc/data/analysis/documentation/Cicerone_Data/LAT_DP.html)

¹¹ <https://fermi.gsfc.nasa.gov/ssc/data/analysis/user/>

¹² <https://fermi.gsfc.nasa.gov/ssc/data/access/lat/BackgroundModels.html>

¹³ https://fermi.gsfc.nasa.gov/ssc/data/analysis/scitools/python_tutorial.html

correspond to the best-fit curves of the short- and long-lasting components, respectively. We fit each component of the energy flux in the LAT light curve with a series of broken and simple PLs. To find the best-fit values of the temporal indexes of PLs, we use the chi-square minimisation χ^2 using the ROOT software package (Brun & Rademakers 1997). Table 1 lists the best-fit temporal indices of the short and long-lasting emissions, including the chi squares ($\chi^2/n.d.f.$).

Data sets from the X-ray Telescope (XRT) instrument on board the *Neil Gehrels Swift Observatory* were retrieved from the publicly available database on the official Swift website.¹⁴ The flux density at 10 keV is transformed to 1 keV using the conversion factor derived in Evans et al. (2010).

3.3 Afterglow evolution: LAT and multi-wavelength observations

We report the best fit values for the short and long LAT components using ROOT Chi-square minimisation χ^2 for the start time, the temporal breaks, and the indexes before and after the break in Table 1. Additionally, with the chi-square minimisation χ^2 of ROOT, we obtain the best-fit values of the X-ray and optical light curves, which we list in Table 2.

3.3.1 GRB 080916C

We note that the short-lasting component occurs during prompt emission ($t_x < T_{90}$) because of the best-fit values of the starting time and the temporal break. Therefore, the RS evolves in the thick-shell regime. The best-fit value of the starting time indicates that the onset of the afterglow was very early. When comparing the best-fit values of the temporal indexes before and after the break of the SSC light curve, we can see that they are consistent with the cooling conditions $\nu_{c,r}^{SSC} < \nu_{LAT} < \nu_{m,r}^{SSC}$ for $t < t_x$ and $\nu_{m,r}^{SSC} < \nu_{LAT} < \nu_{cut,r}^{SSC}$ for $t_x < t$, for $p \approx 2.2$. It should be noted that the decay temporal index is consistent with the high-latitude emission ($\nu_{cut,r}^{SSC} < \nu_{LAT}$); $\beta + 2$. Other cooling conditions of the SSC light curve cannot explain the best-fit values of the temporal indexes.

3.3.1.1 High-energy events. At 3.94 s after the GBM trigger, the first high-energy photon was detected with a measured energy of 161.4 MeV. The energy range of the photons in this burst was extensive, with 283 photons over 100 MeV, 17 exceeding 1 GeV, and 2 exceeding 10 GeV. At 40.5 s after the GBM trigger, the highest-energy photon in the LAT data had a value of 27.43 GeV.

3.3.1.2 Multiwavelength afterglow analysis Analysis of LAT, X-ray, and optical spectra with PL functions leads to spectral indexes of $\beta_{LAT} = \Gamma_{LAT} - 1 = 1.20 \pm 0.06$ (Ajello et al. 2019), $\beta_X = \Gamma_X - 1 = 0.80 \pm 0.40$ ¹⁵ and $\beta_{Opt} = 0.38 \pm 0.20$ (Greiner et al. 2009), respectively. Taking into consideration the LAT analysis of the long-lasting emission and the best-fit values of the temporal and spectral indexes of LAT, X-ray and optical observations, the observed fluxes evolve as $F_{\nu,L} \propto t^{-1.21 \pm 0.06} \nu^{-1.20 \pm 0.06}$, $F_{\nu,X} \propto t^{-1.35 \pm 0.06} \nu^{-0.80 \pm 0.30}$ and $F_{\nu,Opt} \propto t^{-1.41 \pm 0.04} \nu^{-0.38 \pm 0.20}$, respectively. The fact that the temporal (spectral) indexes for the optical and X-ray observations are larger (lower) than for the LAT observations suggests that the closure relations of the synchrotron FS model evolve in a slow-cooling regime through a wind-like medium ($k = 2$) for $p \approx 2.3 \pm 0.3$. Note that the spectral and temporal indices of the optical and X-ray observations are consistent with each other, so the synchrotron closure relations evolve under the condition $\nu_{m,f}^{syn} < \nu_{Opt} < \nu_X < \nu_{c,f}^{syn}$. Similarly, LAT observations indicate that the closure relations evolve under the cooling condition $\nu_{c,f}^{syn} < \nu_{LAT}$.

3.3.2 GRB 090323

We see that the short-lasting emission is present during the prompt episode ($t_x < T_{90}$), so the RS occurs in the thick-shell regime. According to the best-fitting value of the starting time, the onset of the afterglow occurred at the end of the prompt episode. We can infer the evolution of the LAT frequency in the cooling conditions of the SSC light curve by comparing the best-fit values of the temporal indices before and after the break. In this case, ν_{LAT} evolves as $\nu_{c,r}^{SSC} < \nu_{LAT} < \nu_{m,r}^{SSC}$ for $t < t_x$ and as $\nu_{m,r}^{SSC} < \nu_{LAT} < \nu_{cut,r}^{SSC}$ for $t_x < t$, for $p \approx 2.2$. The decay temporal index, $\beta + 2$, agrees with the high-latitude emission ($\nu_{cut,r}^{SSC} < \nu_{LAT}$), which is interesting to note.

3.3.2.1 High-energy events. The first high-energy photon, with a measured energy of 363.4 MeV, was detected 15.05 s after the GBM trigger. In this burst, there were 32 photons with energy over 100 MeV and 5 with energies above 1 GeV. The highest energy photon detected in the LAT data was 7.40 GeV, which occurred 145.91 s after the GBM trigger.

¹⁴ https://www.swift.ac.uk/burst_analyser/00922968/

¹⁵ https://www.swift.ac.uk/xrt_spectra/00020082/

3.3.2.2 Multiwavelength afterglow analysis We use the best-fit spectral indices presented in 2FLGC ($\beta_{\text{LAT}} = 1.30 \pm 0.20$; Ajello et al. 2019) and *Swift*/XRT repository ($\beta_X = 0.80^{+0.34}_{-0.21}$)¹⁶ to evaluate the LAT and X-ray data, respectively. Given the GROND and TLS observations of the optical/NIR afterglow, McBreen et al. (2010) found a spectral index of $\beta_{\text{Opt}} = 0.65 \pm 0.13$, considering the dust extinction similar to Small Magellanic Cloud (SMC) with $A_V^{\text{host}} = 0.14^{+0.04}_{-0.03}$. Using the LAT analysis of the log-lasting emission and the best-fit values of the temporal and spectral indexes of LAT, X-ray, and optical observations, the observed fluxes evolve as $F_{\nu,L} \propto t^{-1.26 \pm 0.40} \nu^{-1.30 \pm 0.10}$, $F_{\nu,X} \propto t^{-1.58 \pm 0.08} \nu^{-0.80^{+0.34}_{-0.21}}$ and $F_{\nu,\text{Opt}} \propto t^{-1.70 \pm 0.04} \nu^{-0.65 \pm 0.13}$, respectively. The fact that the temporal (spectral) index for the optical and X-ray observations is larger (lower) than the LAT data suggests that the closure relations of the synchrotron FS model evolves in a slow cooling regime through a wind-like medium for $p \approx 2.3 \pm 0.3$. It should be noted that the spectral and temporal indices of X-ray and optical observations are compatible with each other, and therefore the synchrotron closure relations evolve under the condition $\nu_{\text{m,f}}^{\text{syn}} < \nu_{\text{Opt}} < \nu_X < \nu_{\text{c,f}}^{\text{syn}}$. Moreover, LAT observations indicate that closure relations evolve under the condition $\nu_{\text{c,f}}^{\text{syn}} < \nu_{\text{LAT}}$.

3.3.3 GRB 090902B

Comparing the best-fit values of the starting time and the temporal break, one can see that this component is observed during the prompt episode ($t_x < T_{90}$), then the RS is in the thick-shell regime. The best fit values of the temporal indices before and after the break of the SSC light curve show that they are consistent with the cooling conditions $\nu_{\text{c,r}}^{\text{SSC}} < \nu_{\text{LAT}} < \nu_{\text{m,r}}^{\text{SSC}}$ for $t < t_x$ and $\nu_{\text{m,r}}^{\text{SSC}} < \nu_{\text{LAT}} < \nu_{\text{c,r}}^{\text{SSC}}$ or $\nu_{\text{cut,r}}^{\text{SSC}} < \nu_{\text{LAT}}$ for $t_x < t$, for $p \approx 2.1$. The best-fit values of the temporal indices cannot be explained by any other cooling conditions of the SSC light curve.

3.3.3.1 High-energy events. At 1.86 s after the GBM trigger, the first high-energy photon was detected with a measured energy of 284.4 MeV. The energy range of the photons in this burst was extensive, with 469 photons over 100 MeV, 67 exceeding 1 GeV, and 7 exceeding 10 GeV. At 81.7 s after the GBM trigger, the highest-energy photon in the LAT data had a measured energy of 39.88 GeV.

3.3.3.2 Multiwavelength afterglow analysis We consider the best-fit spectral index reported in 2FLGC ($\beta_{\text{LAT}} = 0.94 \pm 0.09$; Ajello et al. 2019). Pandey et al. (2010) analysed the afterglow X-ray and UV-optical IR observations of GRB 090902B. After the modelling of the broadband SED, the authors reported spectral indexes of $\beta_X = 0.9 \pm 0.1$ and $\beta_{\text{Opt}} = 0.68 \pm 0.11$ for X-ray and UV-optical-IR observations, respectively, considering the SMC-like dust extinction with $A_V^{\text{host}} = 0.20 \pm 0.06$. Given the analysis of the long-lasting LAT component and the best-fit values of the temporal and spectral indexes of LAT, X-ray, and optical observations, the observed fluxes evolve as $F_{\nu,L} \propto t^{-1.35 \pm 0.06} \nu^{-0.94 \pm 0.09}$, $F_{\nu,X} \propto t^{-1.62 \pm 0.15} \nu^{-0.80^{+0.34}_{-0.21}}$ and $F_{\nu,\text{Opt}} \propto t^{-1.70 \pm 0.04} \nu^{-0.65 \pm 0.13}$, respectively. The fact that the temporal (spectral) indexes for the optical and X-ray observations are larger (lower) than the LAT data suggests that the closure relations of the synchrotron FS model evolves in a slow cooling regime through a wind-like medium for $p \approx 2.3 \pm 0.3$. It should be noted that the spectral and temporal indices of X-ray and optical observations are compatible with each other and, therefore, the synchrotron closure relations evolve under condition $\nu_{\text{m,f}}^{\text{syn}} < \nu_{\text{Opt}} < \nu_X < \nu_{\text{c,f}}^{\text{syn}}$, and the LAT observations evolve under condition $\nu_{\text{c,f}}^{\text{syn}} < \nu_{\text{LAT}}$.

3.3.4 GRB 090926A

Given the best-fit values of the onset time and the temporal break, we see that the short-lasting emission is present during the main episode ($t_x < T_{90}$), so the RS happens in the thick-shell regime. According to the best-fitting value of the starting time, the onset of the afterglow occurred at the end of the prompt episode. We can infer the evolution of the LAT frequency in the cooling conditions of the SSC light curve by comparing the best-fit values of the temporal indices before and after the break. In this case, ν_{LAT} evolves as $\nu_{\text{c,r}}^{\text{SSC}} < \nu_{\text{LAT}} < \nu_{\text{m,r}}^{\text{SSC}}$ for $t < t_x$ and as $\nu_{\text{m,r}}^{\text{SSC}} < \nu_{\text{LAT}} < \nu_{\text{c,r}}^{\text{SSC}}$ for $t_x < t$, for $p \approx 2.2$. We want to emphasise that the temporal index of decay agrees with the high-latitude emission that occurs under the cooling condition $\nu_{\text{cut,r}}^{\text{SSC}} < \nu_{\text{LAT}}$.

3.3.4.1 High-energy events. A 130.6 MeV photon, the first of several high-energy photons, was detected 2.21 s after the GBM trigger. There was a broad range of photon energies in this burst, with 339 having energies larger than 100 MeV, 31 having energies greater than 1 GeV, and 2 having energies greater than 10 GeV. About 24.84 s from the GBM trigger, the LAT data recorded a photon with a peak energy of 19.46 GeV.

3.3.4.2 Multiwavelength afterglow analysis We use the best-fit spectral indices presented in 2FLGC ($\beta_{\text{LAT}} = 1.14 \pm 0.05$; Ajello et al. 2019) and *Swift*/XRT repository ($\beta_X = 0.98^{+0.15}_{-0.14}$)¹⁷ to evaluate the LAT and X-ray data, respectively. Using the afterglow observations of GROND and *Swift* / XRT in three different periods; $\approx T_0 + 84$ ks, $\approx T_0 + 290$ ks and $\approx T_0 + 1.3$ Ms, Rau et al. (2010) reported spectral indexes of $\beta_{\text{Opt}} = 1.02^{+0.03}_{-0.02}$, $1.05^{+0.04}_{-0.02}$ and $1.04^{+0.08}_{-0.06}$, respectively. Given the best-fit values of the temporal and spectral indices of LAT, X-ray, and optical observations, the observed fluxes evolve as $F_{\nu,L} \propto t^{-1.05 \pm 0.22} \nu^{-1.14 \pm 0.05}$, $F_{\nu,X} \propto t^{-1.41 \pm 0.03} \nu^{-0.98^{+0.15}_{-0.14}}$, and $F_{\nu,\text{Opt}} \propto t^{-1.34 \pm 0.06} \nu^{-1.04^{+0.08}_{-0.06}}$, respectively. The fact that the temporal (spectral) indexes for the optical and X-ray observations are larger (lower) than the LAT data suggests that the closure relations of the synchrotron FS model evolve in a slow cooling regime through a wind-like medium for $p \approx 2.3 \pm 0.3$. It should

¹⁶ https://www.swift.ac.uk/xrt_spectra/00020102/

¹⁷ https://www.swift.ac.uk/xrt_spectra/00020113/

be noted that the spectral and temporal indices of X-ray and optical observations are compatible with each other, and therefore the synchrotron closure relations evolve under condition $\nu_{m,f}^{\text{syn}} < \nu_{\text{Opt}} < \nu_X < \nu_{c,f}^{\text{syn}}$, and the LAT observations evolve under condition $\nu_{c,f}^{\text{syn}} < \nu_{\text{LAT}}$.

3.3.5 GRB 110731A

We find that as short-lasting emission is present throughout the main episode, RS must occur in the thick-shell regime ($t_x < T_{90}$), as shown by the best fits of the onset time and the temporal break. By comparing the best-fit values of the temporal indices before and after the break, we can deduce in which cooling conditions of the SSC light curve the LAT frequency evolves. For $t < t_x$, ν_{LAT} evolves as $\nu_{c,r}^{\text{SSC}} < \nu_{\text{LAT}} < \nu_{m,r}^{\text{SSC}}$ when the onset time and the temporal break are not close to each other, and otherwise ν_{LAT} could evolve $\nu_{\text{LAT}} < \nu_{c,r}^{\text{SSC}}$ or $\nu_{c,r}^{\text{SSC}} < \nu_{\text{LAT}}$. For $t_x < t$, ν_{LAT} could evolve under the cooling conditions $\nu_{m,r}^{\text{SSC}} < \nu_{\text{LAT}} < \nu_{c,r}^{\text{SSC}}$ for $p \approx 2.1$. The decay temporal index, $\beta + 2$, agrees with the high-latitude emission, which is interesting to note.

3.3.5.1 High-energy events. The first high-energy photon, with a measured energy of 817.1 MeV, was observed 3.19 s after the GBM trigger. A large variety of photon energies were produced during this burst; 40 photons were more than 100 MeV and 4 more than 1 GeV. The highest energy photon recorded by the LAT occurred 1.93 s after the GBM trigger and had a value of 8.27 GeV.

3.3.5.2 Multiwavelength afterglow analysis We use the best-fit spectral indices presented in 2FLGC ($\beta_{\text{LAT}} = 1.3 \pm 0.2$; Ajello et al. 2019) to analyzed the LAT data. Ackermann et al. (2013b) analysed the X-ray and UV/optical afterglow observations of GRB 110731A. After modelling the broadband SED, the authors reported at 550 s the spectral indexes of $\beta_X = 0.95^{+0.07}_{-0.09}$ and $\beta_{\text{Opt}} = 0.45^{+0.07}_{-0.09}$ for X-ray and UV/optical observations, respectively. Given the LAT analysis and the best-fit values of the temporal and spectral indexes of LAT, late X-ray and optical observations, the closure relations are $F_{\nu,L} \propto t^{-1.14 \pm 0.23} \nu^{-1.3 \pm 0.2}$, $F_{\nu,X} \propto t^{-1.30^{+0.07}_{-0.05}} \nu^{-0.78^{+0.15}_{-0.13}}$, and $F_{\nu,\text{Opt}} \propto t^{-1.38 \pm 0.09} \nu^{-0.45^{+0.07}_{-0.09}}$, respectively. The fact that the temporal (spectral) indexes for the optical and X-ray observations are larger (lower) than the LAT data suggests that the closure relations of the synchrotron FS model evolve in a slow cooling regime through a wind-like medium for $p \approx 2.3 \pm 0.3$. It should be noted that the spectral and temporal indices of X-ray and optical observations are compatible with each other and, therefore, the synchrotron closure relations evolve under condition $\nu_{m,f}^{\text{syn}} < \nu_{\text{Opt}} < \nu_X < \nu_{c,f}^{\text{syn}}$, and the LAT observations evolve under condition $\nu_{c,f}^{\text{syn}} < \nu_{\text{LAT}}$.

3.3.6 GRB 130427A

We find that as short-lasting emission is present throughout the main episode, RS must occur in the thick-shell regime ($t_x < T_{90}$), as shown by the best fits of the onset time and the temporal break. By comparing the best-fit values of the temporal indices before and after the break, we can deduce in which cooling conditions of the SSC light curve the LAT frequency evolves. For $t < t_x$, the *Fermi*/LAT band should evolve under the condition $\nu_{c,r}^{\text{SSC}} < \nu_{\text{LAT}} < \nu_{m,r}^{\text{SSC}}$ when the onset time is near the temporal break. On the other hand, the *Fermi*/LAT band could evolve $\nu_{\text{LAT}} < \nu_{c,r}^{\text{SSC}}$ or $\nu_{c,r}^{\text{SSC}} < \nu_{\text{LAT}}$. For $t_x < t$, the *Fermi* / LAT band could evolve under the cooling condition $\nu_{m,r}^{\text{SSC}} < \nu_{\text{LAT}} < \nu_{c,r}^{\text{SSC}}$ for $p \approx 2.1$. We emphasise that the temporal index of decay agrees with the high-latitude emission and also with a contribution from the FS region.

3.3.6.1 High-energy events. With a measured energy of 189.8 MeV, the first high-energy photon was observed 0.14 s after the GBM trigger. Four hundred sixty-two photons in this burst had energies greater than 100 MeV, 78 were greater than 1 GeV, and 15 were greater than 10 GeV, indicating an extensive range of energies. The most energetic photon seen in the LAT data was clocked in at 94.11 GeV, 243.1 s after the GBM trigger.

3.3.6.2 Multiwavelength afterglow analysis According to the LAT and X-ray observations, we consider the best-fit spectral indexes reported in 2FLGC ($\beta_{\text{LAT}} = 0.99 \pm 0.04$; Ajello et al. 2019) and Swift repository ($\beta_X = 0.495 \pm 0.016$ for $T_0 + 1196$ s and 0.69 ± 0.08 for $T_0 + 44907$ s)¹⁸, respectively. Using UV/optical/IR afterglow observations collected by several ground telescopes, Perley et al. (2014) reported a spectral index evolution between $\beta_{\text{Opt}} = 0.42^{+0.06}_{-0.06}$ and 0.48 ± 0.04 for $t < 1$ day. Given the best-fit values of the temporal and spectral indices of LAT, X-ray, and optical observations, the observed fluxes evolve as $F_{\nu,L} \propto t^{-1.02 \pm 0.2} \nu^{-0.99 \pm 0.04}$, $F_{\nu,X} \propto t^{-1.30 \pm 0.05} \nu^{-0.495^{+0.015}_{-0.016}}$, and $F_{\nu,\text{Opt}} \propto t^{-1.33 \pm 0.04} \nu^{-0.48 \pm 0.04}$, respectively. The fact that the temporal (spectral) index for optical and X-ray observations is larger (lower) than the LAT data suggests that the closure relations of the synchrotron FS model evolve in a slow cooling regime through a wind-like medium for $p \approx 2.3 \pm 0.3$. It should be noted that the spectral and temporal indices of X-ray and optical observations are compatible with each other, and therefore the synchrotron closure relations evolve under the condition $\nu_{m,f}^{\text{syn}} < \nu_{\text{Opt}} < \nu_X < \nu_{c,f}^{\text{syn}} < \nu_{\text{LAT}}$.

3.3.7 GRB 160602B

We see that the short-lived emission is present during the main episode ($t_x < T_{90}$), so the RS evolves in the thick-shell regime. According to the best-fitting value of the starting time, the onset of the afterglow occurred at the end of the prompt episode. We can infer the evolution of

¹⁸ https://www.swift.ac.uk/xrt_spectra/00020113/

the LAT frequency in the cooling conditions of the SSC light curve by comparing the best-fit values of the temporal indices before and after the break. For $t < t_x$, the *Fermi*/LAT band should evolve under the condition $\nu_{c,r}^{\text{SSC}} < \nu_{\text{LAT}} < \nu_{m,r}^{\text{SSC}}$ when the onset time is close to the temporal break. On the other hand, the *Fermi*/LAT band could evolve under conditions $\nu_{\text{LAT}} < \nu_{c,r}^{\text{SSC}}$ or $\nu_{c,r}^{\text{SSC}} < \nu_{\text{LAT}}$. For $t_x < t$, ν_{LAT} could evolve under the cooling condition $\nu_{m,r}^{\text{SSC}} < \nu_{\text{LAT}} < \nu_{c,r}^{\text{SSC}}$ for $p \approx 2.6$. We note that the temporal index of decay agrees with the high-latitude emission $\nu_{c,r}^{\text{SSC}} < \nu_{\text{LAT}}$.

3.3.7.1 High-energy events. The first high-energy photon was detected 25.6 s after the BAT trigger with an energy of 160.2 MeV. The energy range of the photons in this burst was very broad, with 255 photons over 100 MeV, 21 exceeding 1 GeV, and one over 10 GeV. The highest energy photon was observed 346.2 s after the BAT trigger by the LAT instrument and had an energy of 15.3 GeV.

3.3.7.2 Multiwavelength afterglow analysis We use the best-fit temporal and spectral index exhibited in *Swift*/XRT repository ($\alpha_X = 1.27 \pm 0.30$ and $\beta_X = 0.66^{+0.21}_{-0.14}$)¹⁹ to evaluate the X-ray data. After modeling the broadband SED, Fraija et al. (2017a) and Troja et al. (2017) reported spectral indexes of $\beta_{\text{Opt}} = 0.71 \pm 0.12$ and $\beta_{\text{Opt}} = 0.50 \pm 0.05$, after ≈ 3 and 8 hours for optical- NIR observations, respectively, after the trigger time. The late afterglow (the X-ray and optical fluxes) evolves as $F_{\nu,X} \propto t^{-1.27 \pm 0.30} \nu^{-0.66^{+0.21}_{-0.14}}$ and $F_{\nu,\text{Opt}} \propto t^{-0.921 \pm 0.163} \nu^{-0.71 \pm 0.12}$, respectively. Due to the fact that the temporal and spectral indexes for the late optical and X-ray observations are compatible with each other, the synchrotron closure relations can evolve through a wind-like medium for $p \approx 2.3 \pm 0.3$ and under the condition $\nu_{m,f}^{\text{syn}} < \nu_{\text{Opt}} < \nu_X < \nu_{c,f}^{\text{syn}}$.

3.3.8 GRB 180720B

This component occurs during the prompt emission because of the best-fit values of the starting time and the temporal break. Therefore, the RS evolves in the thick-shell regime ($t_x < T_{90}$). We can infer the evolution of the LAT frequency in the cooling conditions of the SSC light curve by comparing the best-fit values of the temporal indices before and after the break. For $t < t_x$, the *Fermi*/LAT band should evolve under the condition $\nu_{c,r}^{\text{SSC}} < \nu_{\text{LAT}} < \nu_{m,r}^{\text{SSC}}$ when the onset time is close to the temporal break. On the other hand, the *Fermi*/LAT band could evolve $\nu_{\text{LAT}} < \nu_{c,r}^{\text{SSC}}$ or $\nu_{c,r}^{\text{SSC}} < \nu_{\text{LAT}}$. For $t_x < t$, the *Fermi* / LAT band could evolve under the cooling condition $\nu_{m,r}^{\text{SSC}} < \nu_{\text{LAT}} < \nu_{c,r}^{\text{SSC}}$ for $p \approx 2.6$. The decay temporal index, $\beta + 2$, agrees with the high-latitude emission, which is interesting to note. This behavior could evolve with high-energy emission from the FS.

3.3.8.1 High-energy events. The first high-energy photon was detected 12.5 s after the BAT trigger with a measured energy of 175.2 MeV. The energy range of the photons in this burst was extensive, with 129 photons over 100 MeV and 8 exceeding 1 GeV. The highest energy photon was observed 142.4 s after the BAT trigger by the LAT instrument and had an energy of 4.9 GeV.

3.3.8.2 Multiwavelength afterglow analysis According to the LAT and X-ray observations, we consider the best-fit spectral indexes reported in 2FLGC ($\beta_{\text{LAT}} = 1.23 \pm 0.10$; Ajello et al. 2019) and *Swift* repository ($\beta_X = 0.697^{+0.010}_{-0.010}$)²⁰, respectively. Using optical observations in the R band collected by several ground telescopes, Fraija et al. (2019c) reported a spectral index evolution between $\beta_{\text{Opt}} = 0.68 \pm 0.06$ and 0.70 ± 0.05 corresponding to the intervals $\sim 2.0 \times 10^2 - 2.5 \times 10^3$ and $\sim 2.5 \times 10^3 - 2.6 \times 10^5$, respectively. Given the best-fit values of the temporal and spectral indexes of the X-ray and optical observations, while the X-ray flux varies from $F_{\nu,X} \propto t^{-0.79 \pm 0.08} \nu^{-0.86 \pm 0.03}$ to $F_{\nu,X} \propto t^{-1.26 \pm 0.06} \nu^{-0.697^{+0.010}_{-0.010}}$, the optical flux evolves $F_{\nu,\text{Opt}} \propto t^{-1.22 \pm 0.02} \nu^{-0.68 \pm 0.06}$ throughout the interval. Before $t \lesssim 2.5 \times 10^3$ s, the temporal (spectral) index for optical observations is larger (lower) than X-ray data, suggesting that the closure relations of the synchrotron FS model evolve in slow-cooling regime through a wind-like medium for $p \approx 2.0 \pm 0.25$. In this case, the synchrotron closure relations evolve under condition $\nu_{m,f}^{\text{syn}} < \nu_{\text{Opt}} < \nu_{c,f}^{\text{syn}} < \nu_X$. After $2.5 \times 10^3 \text{ s} \lesssim t$, the spectral and temporal indices of X-ray and optical observations are compatible with each other, and therefore the synchrotron closure relations evolve under condition $\nu_{m,f}^{\text{syn}} < \nu_{\text{Opt}} < \nu_X < \nu_{c,f}^{\text{syn}}$. We conclude that the temporal break at $\approx 2.5 \times 10^3$ s to the passage of the forward shock cooling break through the *Swift*/XRT band.

3.4 Results and Discussion

All panels in Figure 3 show the LAT, X-ray and optical observations of GRB 080916C, GRB 090323, GRB 090902B, GRB 090926A, GRB 110731A, GRB 130427A, GRB 160625B and GRB 180720B with the best-fit curve of the short- (dotted) and long- (dotted-dashed) lasting components. Total emission is displayed with a solid line. We used Markov-Chain Monte Carlo (MCMC) simulations with the eight parameters used for the complete sample of GRBs to find the best-fit values that describe the multiwavelength observations with the SSC and synchrotron from the reverse and forward shock models. To represent all the data in this case, a total of 15,900 samples and 4,400 tuning steps are used. Figures 4 - 11 show the best-fit values and the median of the posterior distributions of the parameters. In Table 3, the best-fit values are shown in red, and the median of the posterior distributions is presented. Table 4 shows the SSC spectral breaks from reverse shocks, which are estimated with the best-fit values reported in Table 3. The SSC spectral breaks from the RS region are estimated for GRB 080916C, 090323, 090902B,

¹⁹ https://www.swift.ac.uk/xrt_spectra/00020113/

²⁰ https://www.swift.ac.uk/xrt_spectra/00848890/

090926A, 110731A, 130427A, 160625B, and 180720B at 4 (30) s, 100 (315) s, 3 (16) s, 6 (20) s, 6 (20) s, 6 (32) s, 100 (316) s and 63 (200) s for $t < t_x$ ($t_x < t$), respectively. The synchrotron spectral breaks from the FS region are estimated to be 10^5 s. Figure 12 exhibits all photons with energies > 100 MeV and probabilities $> 90\%$ of being associated with each burst. Additionally, we show in red lines the maximum photon energies released by the SSC (dotted) and synchrotron (dashed) from the reverse and forward afterglow models, respectively, estimated with the best-fit values reported in Table 3.

3.4.1 Microphysical parameters

3.4.1.1 ϵ_B -parameter The best-fit values of the magnetic microphysical parameter from the RS lie in the range of $0.01 \lesssim \epsilon_{B_r} \lesssim 0.1$. Taking into account the values of the microphysical parameters, the magnetisation parameter is estimated to be in the range $0.01 \lesssim \sigma \lesssim 0.1$, indicating that the ejecta are moderately magnetic and as a result the RS is expected to be successful. If this was not the case, the acceleration of the particles in RS would be ineffective and RS would not have occurred (Zhang & Kobayashi 2005; Fan et al. 2004). The microphysical parameter of the magnetic field in the FS and RS regions is different. The ratio of these parameters lie in the range of $1 \lesssim \mathcal{R}_B \lesssim 20$.²¹ It has been suggested that the high-energy emission seen in the brightest LAT-detected bursts could be explained by Poynting flux-dominated models with arbitrary magnetization (e.g., see Uhm & Zhang 2014; Zhang & Yan 2011). The values of the magnetisation parameter suggest that a substantial amount of Poynting flux was released by the ejecta during the prompt emission phase, with the internal collision-induced magnetic reconnection and turbulence (ICMART) event being the most likely mechanism that accounts for this behaviour (Zhang & Yan 2011).

3.4.1.2 ϵ_e -parameter The best-fit values of the ϵ_e microphysical parameter in the forward- and RS model are presented in the 7th and 8th rows of Table 3, respectively. For the forward shock, we find $2.8 \times 10^{-3} \lesssim \epsilon_{e_f} \lesssim 0.12$, while for the RS we have $0.03 \lesssim \epsilon_{e_r} \lesssim 0.13$. As a general rule, we notice that $\epsilon_{e_f} < \epsilon_{e_r}$. Moreover, there is a large variation in the ratio of both quantities between each burst. For example, in the case of GRB 110731A we find the largest disparity $\mathcal{R}_e \equiv \epsilon_{e_r}/\epsilon_{e_f} \approx 46$, while for GRB 160625B $\mathcal{R}_e \approx 0.7$, so the variation can occur over several orders of magnitude. It should be noted that an RS is suppressed for $\mathcal{R}_e \ll 1$ (Fraija et al. 2020).

Although it is usually assumed that the electron microphysical parameter in both the RS and the FS has a similar value (Zhang & Kobayashi 2005; Gao et al. 2015), the possibility of them being different has been explored in previous work, such as the one by Panaitescu & Kumar (2004), in which the authors noted that in the case of GRB 990123 for a $k = 0$ model $\epsilon_{e_r} < 0.1\epsilon_{e_f}$, which is not in agreement with our results. However, given the current uncertainties on the acceleration process that energises electrons, it proves difficult to determine a relation between this parameter in both regions.

3.4.2 The post jet-break decay phase

After about $T + 1$ day (Racusin et al. 2009), during the post jet break decay phase, the multi-wavelength light curves would evolve as $F_\nu^{\text{syn}} \propto t^{-p}$, for $v_{m,f}^{\text{syn}} < \nu < v_{c,f}^{\text{syn}}$ or $\max\{v_{m,f}^{\text{syn}}, v_{c,f}^{\text{syn}}\} < \nu$ (see e.g. Fraija et al. 2022), which are different from the temporal decay indexes found for all bursts (Pereyra et al. 2022; Becerra et al. 2019c), except GRB 160625B (Fraija et al. 2017c). This means that, apart from GRB 160625B, they were likely released from a broad outflow with a large half-opening angle, as shown by multi-wavelength measurements which show no indication of late steep decays. Based on the best-fit values of the circumburst density and the kinetic equivalent energies, we find that the jet opening angles become $\gtrsim 10^\circ$, and for GRB 160625B, the value of the jet opening angle is $\theta_j \approx 2.3^\circ$, which is in the typical interval for $\theta_j = 2^\circ - 10^\circ$ (Bloom et al. 2001).

3.4.3 Efficiency of equivalent kinetic energy

The efficiency provides crucial information on the gamma-ray emitting process. The best fit values of the equivalent kinetic energies $10^{53.96^{+1.01}_{-1.05}} \leq E \leq 10^{54.85^{+1.05}_{-1.02}}$ erg and the isotropic energies in gamma-rays reported by the GBM instrument during the prompt episode in the range of $(0.39 \pm 0.09) \times 10^{52} \leq E_{\gamma,\text{iso}} \leq (1.7 \pm 0.1) \times 10^{54}$ erg (Ajello et al. 2019) lead to kinetic efficiencies in the range of $0.01 \lesssim \eta \lesssim 0.36$, which are typical compared to those values reported in the literature (Guetta et al. 2001; Zhang et al. 2007; Kumar & Zhang 2015), and a kinetic efficiency of $\eta \approx 0.02$ for GRB 180720B (Abdalla et al. 2019; Fraija et al. 2019c), which is very low. The atypical value of efficiency for GRB 180720B was calculated considering the isotropic energy reported by GBM during the interval 4.4-53.2 s. If we have considered the isotropic energy reported by the LAT instrument throughout the interval 11.8-625.0 s, the kinetic efficiency would have been $\eta \approx 0.002$. Similarly, the second-lowest efficiency, which corresponds to $\eta = 0.01$. If we had considered the isotropic energy reported by the LAT in the interval 0.1 - 34366.2 s instead of the GBM instrument, the kinetic efficiency would be $\eta \approx 0.06$.

²¹ \mathcal{R}_B is defined as $\epsilon_{B_r}/\epsilon_{B_f}$.

3.4.4 The profile of the circumburst environment

The best-fit values of the wind parameter lie in the range of $10^{-3} \lesssim A_k \lesssim 0.02$, typical for GRBs identified as powerful bursts (Ackermann et al. 2013b; Perley et al. 2014; Vestrand et al. 2014; Fraija et al. 2012; Racusin et al. 2008; Fraija et al. 2017c; Becerra et al. 2017). Recently, Dainotti et al. (2023) considered the GRBs reported in the 2FLGC and analysed the evolution of the relationship between the spectral and temporal indices using closure relations in a stratified environment. They found that the afterglow model without energy injection is preferred over that with energy injection with a clear preference for the cooling condition $\nu > \max\{\nu_c, \nu_m\}$, as derived (see Table 4). Furthermore, the authors reported that the density profiles r^{-k} with $k = 2$ have a higher rate of occurrence.

The best-fit values of the initial bulk Lorentz factor lie in the range $290 \lesssim \Gamma \lesssim 10^3$, which is similar to the values found in other bursts detected by the LAT instrument and those expected in numerical simulations (Tchekhovskoy et al. 2008). Since our GRB sample displayed the most energetic photons, the values of the bulk Lorentz factor are predicted to fall within the same range as the bursts observed by the LAT that are the brightest (Ackermann et al. 2011; Veres & Mészáros 2012; Ackermann et al. 2013b; Abdo et al. 2009b; Ackermann & et al. 2010; Ackermann et al. 2014; Fraija et al. 2019a,c), as found. Given the best-fit values, the critical Lorentz factors are consistent with the thick-shell scenario.

3.4.5 Fraction of the shock-accelerated electrons

In the standard GRB afterglow model, it is assumed that the fraction of electrons accelerated by shock is $\zeta_e \sim 1$. However, the validity of this assumption has been questioned by several authors. For example, Bykov & Meszaros (1996) considered the increase in the electron Lorentz factor taking a value $\zeta_e \sim 10^{-3}$, which would lead to a change in the synchrotron spectrum. On the other hand, Eichler & Waxman (2005) concluded that, while observations suggest that $\zeta_e \sim 1$, the range $m_e/m_p \approx 5 \times 10^{-4} \leq \zeta_e \leq 1$ cannot be ruled out because models with different values of ζ_e in the aforementioned range lead to very similar predictions.

In the last row of Table 3, we present the parameter values of ζ_e that we obtained for our sample of GRBs through our MCMC estimation. We notice that our lowest value is for GRB 080916C with $\zeta_e \approx 0.02$, while the largest corresponds to GRB 180720B with $\zeta_e \approx 0.62$. This means that all estimates are within the allowed range of Eichler & Waxman (2005).

3.4.6 The highest energy photons

Figure 12 shows that with the exception of GRB 110731A, the SSC and synchrotron models radiated in the RS and FS regions cannot explain the highest-energy photons exhibited. Therefore, a different process needs to be invoked to interpret these photons. The number of photons (N_γ) with energy $h\nu$ that reach the *Fermi*-LAT instrument during a specific time interval (Δt) can be estimated considering the effective area of LAT (A) and the observed flux at the determined time. The number of photons is

$$N_\gamma \sim 1 \text{ ph} \left(\frac{h\nu}{10 \text{ GeV}} \right) \left(\frac{10 \text{ s}}{\Delta t} \right) \left(\frac{F_{\nu,j}^{\text{SSC}}}{10^{-9} \frac{\text{erg}}{\text{cm}^2 \text{ s}}} \right) \left(\frac{10^4 \text{ cm}^2}{A} \right). \quad (24)$$

In order to estimate the number of photons we discuss hadronic and SSC scenarios. In the hadronic scenarios, high-energy gamma-ray emission has been interpreted via photo-hadronic interactions; ultrarelativistic protons accelerated in the jet with internal synchrotron photons (Asano et al. 2009; Dermer et al. 2000), inelastic proton-neutron collisions (Mészáros & Rees 2000), and relativistic neutrons with seed photons coming from the outflow (Dermer & Atoyan 2004; Alvarez-Muñiz et al. 2004). Even though GRBs are among the most plausible candidates to accelerate cosmic rays up to ultra-high energies ($\gtrsim 10^{18}$ eV; Waxman 1995; Vietri 1995) and thus, potential candidates for neutrino detection, the IceCube collaboration reported no coincidences between neutrinos and GRBs after analyzing years of data (Abbasi et al. 2022, 2012; Aartsen et al. 2016, 2015). Because of this, we rule out hadronic models as an explanation for the observed properties of GRBs and conclude that the number of hadrons is too small for hadronic interactions to efficiently generate observable gamma-ray signals in GRBs. On the other hand, the SSC scenario has been successfully applied to interpret the highest-energy photons (e.g., see Fraija et al. 2019c; Wang et al. 2019; Zhang 2019; Fraija et al. 2019b, 2021, 2017b). In this scenario, the same electron population can up-scatter synchrotron photons up to higher energies as $h\nu_{i,f}^{\text{SSC}} \sim \gamma_{i,f}^2 h\nu_{i,f}^{\text{syn}}$, reaching a maximum flux of $F_{\text{max},f}^{\text{SSC}} \sim \frac{4\sigma_T nr}{3g(p)} F_{\text{max},f}^{\text{syn}}$ with $r \approx 4c\Gamma^2 t / (1+z)$. The spectral breaks and the maximum flux for SSC emission in the forward shock can be expressed as

$$\begin{aligned} h\nu_{m,f}^{\text{SSC}} &\approx 4.3 \times 10^2 \text{ MeV} \left(\frac{1+z}{2} \right)^{\frac{10-3k}{2(4-k)}} g^4 (2.2) \zeta_e^{-4} \varepsilon_{\text{ef},-1}^4 \varepsilon_{\text{Bf},-2}^{\frac{1}{2}} A_{k,-1}^{-\frac{1}{4-k}} E_{53}^{\frac{6-k}{2(4-k)}} t_2^{-\frac{18-5k}{2(4-k)}}, \\ h\nu_{c,f}^{\text{SSC}} &\approx 4.6 \times 10^2 \text{ eV} \left(\frac{1+z}{2} \right)^{\frac{3(2+k)}{2(4-k)}} \left(\frac{1+Y_f}{2} \right)^{-4} \varepsilon_{\text{Bf},-2}^{-\frac{7}{2}} A_{k,-1}^{-\frac{9}{4-k}} E_{53}^{-\frac{10-7k}{2(4-k)}} t_2^{-\frac{2-5k}{2(4-k)}}, \\ F_{\text{max},f}^{\text{SSC}} &\approx 8.1 \times 10^{-3} \text{ mJy} \left(\frac{1+z}{2} \right)^{\frac{14-k}{2(4-k)}} g^{-1} (2.2) \zeta_e \varepsilon_{\text{Bf},-2}^{\frac{1}{2}} A_{k,-1}^{\frac{5}{4-k}} d_{z,28.3}^{-2} E_{53}^{\frac{5(2-k)}{2(4-k)}} t_2^{\frac{2-3k}{2(4-k)}}. \end{aligned} \quad (25)$$

In the fast- and slow-cooling regime the SSC light curve are given by (Sari & Esin 2001)

$$F_{\nu,f}^{\text{SSC}} \propto \begin{cases} t^{\frac{2-k}{4(4-k)}} \nu^{-\frac{1}{2}}, & \nu_{c,f}^{\text{SSC}} < \nu < \nu_{m,f}^{\text{SSC}}, \\ t^{\frac{2(10-3k)+p(5k-18)}{4(4-k)}} \nu^{-\frac{p}{2}}, & \nu_{m,f}^{\text{SSC}} < \nu, \end{cases} \quad (26)$$

and

$$F_{\nu,f}^{\text{SSC}} \propto \begin{cases} t^{\frac{11(2-k)+p(5k-18)}{4(4-k)}} \nu^{-\frac{p-1}{2}}, & \nu_{\text{m,f}}^{\text{SSC}} < \nu < \nu_{\text{c,f}}^{\text{SSC}}, \\ t^{\frac{2(10-3k)+p(5k-18)}{4(4-k)}} \nu^{-\frac{p}{2}}, & \nu_{\text{c,f}}^{\text{SSC}} < \nu, \end{cases} \quad (27)$$

respectively. For $\nu_{\text{c,f}}^{\text{SSC}} < \nu_{\text{m,f}}^{\text{SSC}}$ and $\nu_{\text{m,f}}^{\text{SSC}} < \nu_{\text{c,f}}^{\text{SSC}}$, the spectral breaks due to the KN effect are

$$h\nu_{\text{KN,m,f}}^{\text{SSC}} \simeq 1.2 \times 10^2 \text{ GeV} \left(\frac{1+z}{2} \right)^{-\frac{1}{4-k}} g(2.2) \zeta_e^{-1} \varepsilon_{e,f,-1} A_{k,-1}^{-\frac{1}{4-k}} E_{53}^{\frac{1}{4-k}} t_2^{-\frac{3-k}{4-k}}, \quad (28)$$

$$h\nu_{\text{KN,c,f}}^{\text{SSC}} \simeq 3.8 \text{ GeV} \left(\frac{1+z}{2} \right)^{-\frac{3}{4-k}} \left(\frac{1+Y_f}{2} \right)^{-1} \varepsilon_{\text{Bf},-2}^{-1} A_{k,-1}^{-\frac{3}{4-k}} E_{53}^{-\frac{1-k}{4-k}} t_2^{-\frac{1-k}{4-k}}. \quad (29)$$

The maximum energy radiated by the SSC process is estimated by $h\nu_{\text{max,f}}^{\text{SSC}} \simeq \gamma_{\text{max,f}}^2 (h\nu_{\text{max,f}}^{\text{syn}})$.

Given the best-fit values listed in Table 3, the number of photons at the highest energies are: 0.9, 0.2, 1.2, 1.6, 31.2, 0.6 and 1.7 for GRB 080916C, 090323, 090902B, 090926A, 130427A, 160625B and 180720B, respectively. Therefore, although there is an excess from GRB 130427A due to the spectral index, the most energetic photons could be explained by the SSC mechanism from the forward shock.

3.4.7 Spectral breaks in the Klein-Nishina regime

The values of the spectral breaks derived from the best fit parameters and listed in Table 4 show that, with the exception of GRB 090323 and GRB 090926A, the KN effects are neglected. For GRB 090323, the spectral breaks are in the order $\nu_{\text{c}}^{\text{syn}} < h\nu_{\text{KN}}^{\text{syn}}(\gamma_*) < \nu_{\text{m}}^{\text{syn}} < \nu_{\text{KN}}^{\text{syn}}(\gamma_{\text{m}})$ with $h\nu_{\text{m,r}}^{\text{syn}} = 1.1 \times 10^3 \text{ eV}$, $h\nu_{\text{c,r}}^{\text{syn}} = 8.2 \text{ eV}$, $h\nu_{\text{KN,m,r}}^{\text{syn}} = 1.2 \times 10^5 \text{ eV}$, $h\nu_{\text{KN,c,r}}^{\text{syn}} = 6.3 \times 10 \text{ eV}$ and $h\nu_{\text{KN,r}}^{\text{syn}}(\gamma_*) = 3.5 \times 10^2 \text{ eV}$. In this case, the Compton parameter was recalculated (for details, see Wang et al. 2010). A similar procedure was developed for GRB 090926A.

4 SUMMARY

We have extended the SSC RS model in a medium of constant density initially proposed to explain the LAT GeV flare observed in GRB 160509A (Fraija et al. 2020). In the current model, we have generalised and derived the SSC light curves from the RS region in the thick and thin shell scenarios for a stratified environment with a density profile $\propto r^{-k}$ with $0 \leq k < 3$, including the maximum energy radiated by this process in both regimes. In order to apply our theoretical model to a sample of eight bursts (GRB 080916C, 090323, 090902B, 090926A, 110731A, 130427A, 160625B and 180720B) reported in the 2FLGC (Ajello et al. 2019), which exhibited interesting short-lasting bright peaks, we have obtained the Fermi-LAT light curves together with the photons with energies $\geq 100 \text{ MeV}$ associated with each burst. We have used the multiwavelength observations to constrain the parameters in the model and fitted the LAT light curves of the sample of GRBs with a joint model which considers synchrotron and SSC emission from both the FS and the RS through MCMC simulations. We have shown that the emission in the thick-shell scenario could describe the short-lasting bright peaks exhibited in our GRB sample. Because the shock crossing time is smaller than the duration of the prompt emission in the thick-shell regime, the bright peak in this regime is expected at the beginning of the FS emission. By contrast, if the shock crossing time is longer than the duration of the prompt emission in the thin-shell scenario, the bright peak is separated from the prompt emission and expected during the FS emission.

We show that at the beginning of the LAT observations, the SSC flux from the RS region is larger than the synchrotron flux from the FS. Therefore, the closure relations of the synchrotron FS model are not expected when the LAT light curves are a superposition of the SSC and synchrotron from RS and FS. It is worth highlighting that, depending on the parameter values, the short-lasting bright peaks could be hidden by the long-lasting emission.

The best-fit values of the magnetic microphysical parameter for our sample of bursts were consistent with moderate magnetic ejecta and $\mathcal{R}_e \ll 1$, which indicated that the RS was successful. With respect to the electron microphysical parameter, we noticed that there was a large variation between the values of the FS and the RS, which suggests that the acceleration mechanisms are substantially different. We found that in all bursts except GRB 160625B, the radiation was most likely released from a broad outflow with a large opening angle. We calculated the kinetic efficiency for every burst in our sample and found that most of the values are consistent with those of previous studies. However, GRB 180720B presented a value that was far below the standard. We have calculated the best-fit values of the wind parameter for our sample of bursts. We have found that all of the results are consistent with powerful GRBs. This conclusion is further strengthened by the fact that our sample displayed the most energetic photons, which are also expected from the most powerful bursts. We tested the assumption that the fraction of accelerated electrons in the shock is close to unity. We have found that this is not the case in all the bursts of our sample. However, an accurate determination of this parameter is difficult, as different values lead to similar predictions.

Given the best-fit values, we have shown that the first high-energy photons are consistent with the starting time of the short-lasting emission. Similarly, we have shown that, unlike GRB 110731A, the highest energy photon cannot be described neither by the standard synchrotron emission from RS nor from the FS, and a different process from the ones considered have to be invoked to interpret these photons. We show that unlike GRB 090323 the highest-energy photons are consistent with SSC from the FS region. We have shown that in all but two bursts from our

sample, KN effects are neglected. However, in the case of GRB 090323 and GRB 090926A, they are important, and so we have recalculated the Compton parameter appropriately in both cases.

ACKNOWLEDGEMENTS

NF acknowledges financial support from UNAM-DGAPA-PAPIIT through grant IN106521. M.G.D. acknowledges funding from the AAS Chretienne Fellowship and the MINIATURA2 grant. R.L.B. acknowledges support from the CONAHCyT postdoctoral fellowship and the financial support from UNAM-DGAPA-PAPIIT through grant IN105921.

DATA AVAILABILITY

The data underlying this article will be shared on reasonable request to the corresponding author.

REFERENCES

- Aartsen M. G., et al., 2015, *ApJ*, **805**, L5
Aartsen M. G., et al., 2016, *ApJ*, **824**, 115
Abbasi R., et al., 2012, *Nature*, **484**, 351
Abbasi R., et al., 2022, arXiv e-prints, p. [arXiv:2205.11410](https://arxiv.org/abs/2205.11410)
Abdalla H., et al., 2019, *Nature*, **575**, 464
Abdo A. A., et al., 2009a, *Science*, **323**, 1688
Abdo A. A., et al., 2009b, *ApJ*, **706**, L138
Abdollahi S., et al., 2022, *ApJS*, **260**, 53
Ackermann M., et al. 2010, *ApJ*, **716**, 1178
Ackermann M., et al., 2011, *ApJ*, **729**, 114
Ackermann M., et al., 2013a, *ApJS*, **209**, 11
Ackermann M., et al., 2013b, *ApJ*, **763**, 71
Ackermann M., et al., 2014, *Science*, **343**, 42
Ajello M., et al., 2018, *ApJ*, **863**, 138
Ajello M., Arimoto M., Axelsson M., Baldini L., Barbiellini G., Bastieri D., et al. 2019, *The Astrophysical Journal*, **878**, 52
Alvarez-Muñiz J., Halzen F., Hooper D., 2004, *ApJ*, **604**, L85
Asano K., Guiriec S., Mészáros P., 2009, *ApJ*, **705**, L191
Band D., et al., 1993, *ApJ*, **413**, 281
Barniol Duran R., Kumar P., 2011, *MNRAS*, **412**, 522
Barthelmy S. D., et al., 2018, GRB Coordinates Network, Circular Service, No. 22998, #1 (2018), 22998
Becerra R. L., et al., 2017, *ApJ*, **837**, 116
Becerra R. L., et al., 2019a, *ApJ*, **872**, 118
Becerra R. L., et al., 2019b, *ApJ*, **881**, 12
Becerra R. L., et al., 2019c, *ApJ*, **887**, 254
Bersier D., 2011, GRB Coordinates Network, 12216, 1
Bissaldi E., 2009, GRB Coordinates Network, 9933, 1
Bissaldi E., Racusin J. L., 2018, GRB Coordinates Network, Circular Service, No. 22980, #1 (2018), 22980
Bloom J. S., Frail D. A., Sari R., 2001, *AJ*, **121**, 2879
Brun R., Rademakers F., 1997, *Nuclear Instruments and Methods in Physics Research A*, **389**, 81
Burns E., 2016, GRB Coordinates Network, 19581
Bykov A. M., Meszaros P., 1996, *ApJ*, **461**, L37
Cavallo G., Rees M. J., 1978, *MNRAS*, **183**, 359
Cenko S. B., et al., 2011, *ApJ*, **732**, 29
Chakrabarti S. K., et al., 2009, GRB Coordinates Network, Circular Service, No. 109, #1 (2009), 10009
Chevalier R. A., Li Z.-Y., 2000, *ApJ*, **536**, 195
Chornock R., Perley D. A., Cenko S. B., Bloom J. S., 2009, GRB Coordinates Network, 9028
Clemens C., Rossi A., Greiner J., McBreen S., Kruehler T., Yoldas A., Yoldas A. K., Szokoly G., 2008, GRB Coordinates Network, 8272
Cucchiara A., Fox D. B., Tanvir N., Berger E., 2009, GRB Coordinates Network, 9873
Dainotti M., Levine D., Fraija N., Warren D., Veres P., Sourav S., 2023, *Galaxies*, **11**, 25
Dermer C. D., Atayan A., 2004, *A&A*, **418**, L5
Dermer C. D., Böttcher M., Chiang J., 2000, *ApJ*, **537**, 255
Dirirsa F., Vianello G., Racusin J., Axelsson M., 2016, GRB Coordinates Network, 19586
Eichler D., Waxman E., 2005, *ApJ*, **627**, 861
Evans P. A., et al., 2010, *A&A*, **519**, A102
Fan Y., Piran T., 2006, *MNRAS*, **369**, 197
Fan Y. Z., Wei D. M., Wang C. F., 2004, *A&A*, **424**, 477
Flores H., et al., 2013, GRB Coordinates Network, 14491, 1
Fraija N., González M. M., Lee W. H., 2012, *ApJ*, **751**, 33
Fraija N., Lee W., Veres P., 2016, *ApJ*, **818**, 190
Fraija N., et al., 2017a, *ApJ*, **848**, 15
Fraija N., Lee W. H., Araya M., Veres P., Barniol Duran R., Guiriec S., 2017b, *ApJ*, **848**, 94
Fraija N., et al., 2017c, *ApJ*, **848**, 15
Fraija N., Dichiara S., Pedreira A. C. C. d. E. S., Galvan-Gamez A., Becerra R. L., Barniol Duran R., Zhang B. B., 2019a, *ApJ*, **879**, L26
Fraija N., Barniol Duran R., Dichiara S., Beniamini P., 2019b, *ApJ*, **883**, 162
Fraija N., et al., 2019c, *ApJ*, **885**, 29
Fraija N., Laskar T., Dichiara S., Beniamini P., Duran R. B., Dainotti M. G., Becerra R. L., 2020, *ApJ*, **905**, 112
Fraija N., Veres P., Beniamini P., Galvan-Gamez A., Metzger B. D., Barniol Duran R., Becerra R. L., 2021, *ApJ*, **918**, 12
Fraija N., Galvan-Gamez A., Betancourt Kamenetskaia B., Dainotti M. G., Dichiara S., Veres P., Becerra R. L., do E. S. Pedreira A. C. C., 2022, *ApJ*, **940**, 189
Gao H., Wang X.-G., Mészáros P., Zhang B., 2015, *ApJ*, **810**, 160
Goldstein A., van der Horst A., 2008, GRB Coordinates Network, 8245

- Golenetskii S., et al., 2009, GRB Coordinates Network, [9959](#), 1
- Golenetskii S., et al., 2011, GRB Coordinates Network, [12223](#), 1
- Golenetskii S., et al., 2013, GRB Coordinates Network, [14487](#), 1
- Granot J., Sari R., 2002, *ApJ*, [568](#), 820
- Greiner J., et al., 2009, *A&A*, [498](#), 89
- Guetta D., Spada M., Waxman E., 2001, *ApJ*, [557](#), 399
- Hanabata Y., et al., 2011, GRB Coordinates Network, [12244](#), 1
- Izzo L., Auchettl K., Hjorth J., De Colle F., Gall C., Angus C. R., Raimundo S. I., Ramirez-Ruiz E., 2020, *A&A*, [639](#), L11
- Kawamuro T., et al., 2013, GRB Coordinates Network, [14462](#), 1
- Kennea J. A., Stratta G., 2009, GRB Coordinates Network, [9868](#)
- Kennea J., Evans P., Goad M., 2009, GRB Coordinates Network, [9024](#)
- Kobayashi S., 2000, *ApJ*, [545](#), 807
- Kobayashi S., Sari R., 2000, *ApJ*, [542](#), 819
- Kobayashi S., Zhang B., 2003, *ApJ*, [597](#), 455
- Kobayashi S., Zhang B., 2007, *ApJ*, [655](#), 973
- Kobayashi S., Piran T., Sari R., 1999, *ApJ*, [513](#), 669
- Kouveliotou C., et al., 2013, *ApJ*, [779](#), L1
- Kumar P., Barniol Duran R., 2009, *MNRAS*, [400](#), L75
- Kumar P., Barniol Duran R., 2010, *MNRAS*, [409](#), 226
- Kumar P., Zhang B., 2015, *Phys. Rep.*, [561](#), 1
- Kumar P., Narayan R., Johnson J. L., 2008, *Science*, [321](#), 376
- Levan A. J., Cenko S. B., Perley D. A., Tanvir N. R., 2013, GRB Coordinates Network, [14455](#), 1
- Liang E.-W., et al., 2013, *ApJ*, [774](#), 13
- Malesani D., et al., 2009, GRB Coordinates Network, [9942](#), 1
- Malesani D., Leloudas G., Xu D., de Ugarte Postigo A., Hjorth J., Jakobsson P., Nielsen M. B., 2011, GRB Coordinates Network, [12220](#), 1
- Maselli A., et al., 2014, *Science*, [343](#), 48
- Maxham A., Zhang B.-B., Zhang B., 2011, *MNRAS*, [415](#), 77
- McBreen S., et al., 2010, *A&A*, [516](#), A71
- Mészáros P., Rees M. J., 1997, *ApJ*, [476](#), 232
- Mészáros P., Rees M. J., 2000, *ApJ*, [541](#), L5
- Moskvitin A. S., Sokolov V. V., Spiridonova O. I., Andreev M. V., Sergeev A. V., Parakhin N. A., 2011, GRB Coordinates Network, [12333](#), 1
- Nakar E., Ando S., Sari R., 2009, *ApJ*, [703](#), 675
- Noda K., et al., 2009, GRB Coordinates Network, [9951](#)
- Oates S. R., et al., 2011, GRB Coordinates Network, [12215](#), 1
- Ohno M., Cutini S., McEnery J., Chiang J., Koerding E., 2009, GRB Coordinates Network, [9021](#)
- Palmer D., Siegel M. H., Burrows D. N., et al., 2018, GRB Coordinates Network, Circular Service, No. 22973, #1 (2018), [22973](#)
- Panaitescu A., Kumar P., 2000, *ApJ*, [543](#), 66
- Panaitescu A., Kumar P., 2004, *MNRAS*, [353](#), 511
- Panaitescu A., Vestrand W. T., Woźniak P., 2014, *ApJ*, [788](#), 70
- Pandey S. B., et al., 2010, *ApJ*, [714](#), 799
- Pereyra M., et al., 2022, *MNRAS*, [511](#), 6205
- Perley D., 2013, GRB Coordinates Network, [14494](#), 1
- Perley D. A., et al., 2014, *ApJ*, [781](#), 37
- Perri M., Stratta G., 2009, GRB Coordinates Network, [9031](#)
- Perri M., Preger B., Stratta G., 2008, GRB Coordinates Network, [8261](#)
- Piran T., Nakar E., 2010, *ApJ*, [718](#), L63
- Planck Collaboration Aghanim N., Akrami Y., Ashdown M., Aumont J., Baccigalupi C., et al. 2020, *A&A*, [641](#), A6
- Pozanenko A., Minaev P., Volnova A., 2013, GRB Coordinates Network, [14484](#), 1
- Racusin J. L., et al., 2008, *Nature*, [455](#), 183
- Racusin J. L., et al., 2009, *ApJ*, [698](#), 43
- Rau A., et al., 2010, *ApJ*, [720](#), 862
- Roberts O. J., Meegan C., 2018, GRB Coordinates Network, Circular Service, No. 22981, #1 (2018), [22981](#)
- Sari R., Esin A. A., 2001, *ApJ*, [548](#), 787
- Sari R., Piran T., 1999, *ApJ*, [517](#), L109
- Sari R., Piran T., Narayan R., 1998, *ApJ*, [497](#), L17
- Sasada M., Nakaoka T., Kawabata M., Uchida N., Yamazaki Y., Kawabata K. S., 2018, GRB Coordinates Network, Circular Service, No. 22977, #1 (2018), [22977](#)
- Smith D. M., Csillaghy A., Hurley K., Hudson H., Boggs S., Inglis A., 2013, GRB Coordinates Network, [14590](#), 1
- Swenson C. A., Siegel M. H., 2009, GRB Coordinates Network, [9869](#)
- Tanvir N. R., Wiersema K., Levan A. J., Cenko S. B., Geballe T., 2011, GRB Coordinates Network, [12225](#), 1
- Tchekhovskoy A., McKinney J. C., Narayan R., 2008, *MNRAS*, [388](#), 551
- Troja E., Lipunov V. M., Mundell C. G., et al. 2017, *Nature*, [547](#), 425
- Uhm Z. L., Zhang B., 2014, *Nature Physics*, [10](#), 351
- Veres P., Mészáros P., 2012, *ApJ*, [755](#), 12
- Verrecchia F., et al., 2013, GRB Coordinates Network, [14515](#), 1
- Vestrand W. T., et al., 2006, *Nature*, [442](#), 172
- Vestrand W. T., et al., 2014, *Science*, [343](#), 38
- Vietri M., 1995, *ApJ*, [453](#), 883

- Vreeswijk P. M., et al., 2018, GRB Coordinates Network, Circular Service, No. 22996, #1 (2018), [22996](#)
- Wang X.-Y., He H.-N., Li Z., Wu X.-F., Dai Z.-G., 2010, *ApJ*, **712**, 1232
- Wang X.-Y., Liu R.-Y., Zhang H.-M., Xi S.-Q., Zhang B., 2019, *ApJ*, **884**, 117
- Waxman E., 1995, *Physical Review Letters*, **75**, 386
- Weinberg S., 1972, *Gravitation and Cosmology*
- Xu D., Malesani D., Fynbo J. P. U., Tanvir N. R., Levan A. J., Perley D. A., 2016, GRB Coordinates Network, [19600](#)
- Yi S.-X., Wu X.-F., Dai Z.-G., 2013, *ApJ*, **776**, 120
- Zauderer A., Berger E., Frail D. A., 2011, GRB Coordinates Network, [12227](#), 1
- Zhang B., 2019, arXiv e-prints, p. [arXiv:1911.09862](#)
- Zhang B., Kobayashi S., 2005, *ApJ*, **628**, 315
- Zhang B., Mészáros P., 2001, *ApJ*, **559**, 110
- Zhang B., Yan H., 2011, *ApJ*, **726**, 90
- Zhang B., et al., 2007, *ApJ*, **655**, 989
- Zhang B.-B., et al., 2016, preprint, ([arXiv:1612.03089](#))
- von Kienlin A., 2013, GRB Coordinates Network, [14473](#), 1

Table 1. The best-fit values for the modeling of the short and long-lasting components of the LAT light curves of our GRB sample using PL functions.

Event	LAT	Parameter	Best-fit value	χ^2/ndf
GRB 080916C	Short-lasting component	$\alpha_{\text{rL,bb}}$	-1.05 ± 0.84	1.22
		$\alpha_{\text{rL,ab}}$	3.53 ± 0.70	
		$T_{\text{a}}(\text{s})$	2.40 ± 2.20	
		$t_{\text{r,pk}}(\text{s})$	5.76 ± 0.84	
	Long-lasting component	$\alpha_{L,1}$	0.54 ± 0.27	1.18
		$\alpha_{L,2}$	1.47 ± 0.10	
		$t_{\text{fl,br}}(\text{s})$	22.08 ± 0.02	
		α_L	1.21 ± 0.06	1.12
GRB 090323	Short-lasting component	$\alpha_{\text{rL,bb}}$	-1.11 ± 0.74	0.96
		$\alpha_{\text{rL,ab}}$	4.00 ± 1.90	
		$T_{\text{a}}(\text{s})$	55.19 ± 50.25	
		$t_{\text{r,pk}}(\text{s})$	106.60 ± 72.82	
	Long-lasting component	$\alpha_{L,1}$	1.84 ± 1.12	0.86
		$\alpha_{L,2}$	1.00 ± 0.70	
		$t_{\text{fl,br}}(\text{s})$	576.10 ± 798.60	
		α_L	1.26 ± 0.40	0.67
GRB 090902B	Short-lasting component	$\alpha_{\text{rL,bb}}$	-2.00 ± 1.86	0.92
		$\alpha_{\text{rL,ab}}$	1.77 ± 0.39	
		$T_{\text{a}}(\text{s})$	4.52 ± 1.22	
		$t_{\text{r,pk}}(\text{s})$	8.74 ± 0.52	
	Long-lasting component	$\alpha_{L,1}$	1.90 ± 0.2	1.45
		$\alpha_{L,2}$	1.30 ± 0.01	
		$t_{\text{fl,br}}(\text{s})$	100 ± 0.08	
		α_L	1.35 ± 0.06	1.32
GRB 090926A	Short-lasting component	$\alpha_{\text{rL,bb}}$	-1.37 ± 0.96	0.92
		$\alpha_{\text{rL,ab}}$	4.00 ± 1.82	
		$T_{\text{a}}(\text{s})$	3.00 ± 1.81	
		$t_{\text{r,pk}}(\text{s})$	6.35 ± 0.23	
	Long-lasting component	$\alpha_{L,1}$	1.65 ± 0.10	1.43
		$\alpha_{L,2}$	1.08 ± 0.10	
		$t_{\text{fl,br}}(\text{s})$	106.5 ± 0.08	
		α_L	1.05 ± 0.22	1.38
GRB 110731A	Short-lasting component	$\alpha_{\text{rL,bb}}$	-1.50 ± 1.05	1.34
		$\alpha_{\text{rL,ab}}$	2.67 ± 0.062	
		$T_{\text{a}}(\text{s})$	2.63 ± 1.75	
		$t_{\text{r,pk}}(\text{s})$	5.62 ± 0.03	
	Long-lasting component	$\alpha_{L,1}$	1.57 ± 0.40	0.79
		$\alpha_{L,2}$	2.04 ± 1.34	
		$t_{\text{L,br}}(\text{s})$	71.64 ± 0.54	
		α_L	1.14 ± 0.23	1.76
GRB 130427A	Short-lasting component	$\alpha_{\text{rL,bb}}$	-0.71 ± 0.28	1.07
		$\alpha_{\text{rL,ab}}$	2.00 ± 0.60	
		$T_{\text{a}}(\text{s})$	1.01 ± 0.76	
		$t_{\text{r,pk}}(\text{s})$	19.78 ± 0.01	
	Long-lasting component	$\alpha_{L,1}$	0.81 ± 0.05	0.89
		$\alpha_{L,2}$	1.67 ± 0.52	
		$t_{\text{fl,br}}(\text{s})$	1182.00 ± 1071.00	
		α_L	1.27 ± 0.20	1.08
GRB 160625B	Short-lasting component	$\alpha_{\text{rL,bb}}$	-0.94 ± 0.45	0.87
		$\alpha_{\text{rL,ab}}$	2.50 ± 1.73	
		$T_{\text{a}}(\text{s})$	63.20 ± 11.96	
		$t_{\text{r,pk}}(\text{s})$	130.20 ± 18.96	
GRB 180720B	Short-lasting component	$\alpha_{\text{rL,bb}}$	-0.71 ± 0.28	1.15
		$\alpha_{\text{rL,ab}}$	1.92 ± 0.20	
		$T_{\text{a}}(\text{s})$	31.03 ± 4.16	
		$t_{\text{r,pk}}(\text{s})$	65.78 ± 0.21	
		$\alpha_{\text{rL,ab,1}}$	1.420 ± 0.60	1.18
		$\alpha_{\text{rL,ab,2}}$	3.15 ± 0.60	
		$t_{\text{r,ab}}(\text{s})$	281.84 ± 2.24	

 This paper has been typeset from a \LaTeX file prepared by the author.

Table 2. The best-fit values found from modeling the X-ray and optical light curves using PL functions from our GRB sample.

Event	Band	Parameter	Best-fit value	χ^2/ndf
GRB 080916C	X-rays	α_X	1.35 ± 0.06	1.16
	Optical	α_{opt}	1.41 ± 0.04	1.21
GRB 090323	X-rays	α_X	1.58 ± 0.08	1.08
	Optical	α_{opt}	1.70 ± 0.04	1.15
GRB 090902B	X-rays	α_X	1.62 ± 0.15	0.91
	Optical	α_{opt}	1.70 ± 0.04	1.23
GRB 090926A	X-Rays	α_X	1.41 ± 0.03	1.47
	Optical	α_{opt}	1.34 ± 0.06	1.31
GRB 110731A	X-Rays	$\alpha_{X,1}$	1.15 ± 0.02	1.61
		$\alpha_{X,2}$	1.30 ± 0.03	
		$t_{f_{X,\text{br}}} \text{ (s)}$	$(3.00 \pm 0.98) \times 10^3$	
	Optical	α_{opt}	1.38 ± 0.09	1.54
GRB 130427A	X-Rays	$\alpha_{X,1}$	1.23 ± 0.04	2.23
		$\alpha_{X,2}$	1.30 ± 0.05	
		$t_{f_{X,\text{br}}} \text{ (s)}$	$(2.36 \pm 0.72) \times 10^4$	
	Optical	$\alpha_{\text{opt},1}$	1.16 ± 0.12	1.63
		$\alpha_{\text{opt},2}$	0.89 ± 0.01	
		$\alpha_{\text{opt},3}$	1.33 ± 0.04	
		$t_{f_{O,\text{br}_1}} \text{ (s)}$	$(1.78 \pm 0.02) \times 10^3$	
	$t_{f_{O,\text{br}_2}} \text{ (s)}$	$(4.50 \pm 0.01) \times 10^4$		
GRB 160625B	X-Rays	$\alpha_{X,1}$	1.15 ± 0.13	1.65
		$\alpha_{X,2}$	1.27 ± 0.30	
		$t_{f_{X,\text{br}}} \text{ (s)}$	$(3.12 \pm 0.91) \times 10^3$	
	Optical	α_{opt}	0.921 ± 0.163	1.21
GRB 180720B	X-Rays	$\alpha_{X,1}$	0.79 ± 0.08	0.92
		$\alpha_{X,2}$	1.26 ± 0.06	
		$t_{f_{X,\text{br}}} \text{ (s)}$	$(2.36 \pm 0.72) \times 10^3$	
	Optical	$\alpha_{\text{opt},1}$	1.16 ± 0.12	1.62
		$\alpha_{\text{opt},2}$	0.89 ± 0.01	
		$\alpha_{\text{opt},3}$	1.22 ± 0.02	
		$t_{f_{O,\text{br}_1}} \text{ (s)}$	$(1.78 \pm 0.02) \times 10^3$	
	$t_{f_{O,\text{br}_2}} \text{ (s)}$	$(4.50 \pm 0.01) \times 10^4$		

Table 3. Median values of parameters of our GRB sample with symmetrical quantiles. The SSC and synchrotron models from reverse and forward region, respectively are used to constrain the parameters.

GRB	080916C	090323	090902B	090926A	110731A	130427A	160625B	180720B
$\log_{10}(E/\text{erg})$	$54.85^{+1.05}_{-1.02}$	$53.96^{+1.01}_{-1.05}$	$54.53^{+1.01}_{-1.03}$	$53.83^{+1.03}_{-0.99}$	$53.87^{+0.95}_{-1.06}$	$54.14^{+1.00}_{-1.03}$	$54.29^{+1.03}_{-1.00}$	$54.36^{+1.00}_{-0.95}$
$\log_{10}(A_k)$	$-2.83^{+1.13}_{-0.96}$	$-2.29^{+1.05}_{-1.06}$	$-2.82^{+1.01}_{-1.01}$	$-2.21^{+1.02}_{-0.99}$	$-1.77^{+0.84}_{-1.06}$	$-1.96^{+0.92}_{-1.01}$	$-2.19^{+1.10}_{-1.15}$	$-1.68^{+1.06}_{-0.98}$
$\log_{10}(\Gamma)$	$2.80^{+1.09}_{-0.98}$	$2.92^{+0.99}_{-0.96}$	$2.94^{+1.09}_{-0.99}$	$2.92^{+1.00}_{-0.85}$	$2.54^{+0.87}_{-0.96}$	$2.52^{+1.05}_{-1.04}$	$2.46^{+1.06}_{-0.91}$	$2.46^{+0.89}_{-0.99}$
p	$2.22^{+0.92}_{-1.01}$	$2.68^{+1.08}_{-0.98}$	$2.27^{+1.03}_{-1.02}$	$2.50^{+1.14}_{-0.98}$	$2.35^{+1.04}_{-1.08}$	$2.10^{+0.98}_{-1.00}$	$2.16^{+0.96}_{-1.10}$	$2.09^{+1.03}_{-0.93}$
$\log_{10}(\epsilon_{B_r})$	$-1.54^{+1.07}_{-1.09}$	$-2.13^{+1.03}_{-0.96}$	$-2.05^{+1.05}_{-1.16}$	$-1.86^{+0.91}_{-1.08}$	$-2.20^{+1.02}_{-1.05}$	$-2.64^{+1.09}_{-1.08}$	$-2.36^{+0.95}_{-1.02}$	$-2.22^{+1.04}_{-1.05}$
$\log_{10}(\epsilon_{B_f})$	$-1.32^{+0.95}_{-0.88}$	$-1.03^{+0.94}_{-1.01}$	$-0.96^{+1.04}_{-0.98}$	$-0.98^{+1.00}_{-0.99}$	$-1.99^{+1.04}_{-1.05}$	$-1.48^{+1.00}_{-1.07}$	$-1.06^{+0.98}_{-1.06}$	$-1.54^{+1.01}_{-1.10}$
$\log_{10}(\epsilon_{e_f})$	$-1.84^{+0.93}_{-1.04}$	$-1.24^{+1.11}_{-1.03}$	$-1.38^{+0.94}_{-1.03}$	$-1.15^{+0.91}_{-0.99}$	$-2.55^{+0.85}_{-0.94}$	$-1.76^{+0.95}_{-0.96}$	$-0.92^{+0.98}_{-1.02}$	$-2.02^{+0.97}_{-0.92}$
$\log_{10}(\epsilon_{e_r})$	$-1.25^{+1.11}_{-1.01}$	$-1.11^{+1.01}_{-1.04}$	$-1.10^{+1.13}_{-0.99}$	$-1.04^{+1.07}_{-0.92}$	$-0.89^{+0.93}_{-1.06}$	$-1.44^{+0.90}_{-0.98}$	$-1.11^{+1.05}_{-0.91}$	$-1.51^{+0.96}_{-0.92}$
$\log_{10}(\zeta_e)$	$-1.81^{+0.97}_{-1.09}$	$-0.91^{+1.00}_{-1.02}$	$-0.47^{+1.00}_{-0.93}$	$-0.90^{+1.00}_{-1.11}$	$-0.16^{+1.02}_{-1.10}$	$-0.81^{+0.94}_{-0.97}$	$-1.20^{+1.07}_{-0.98}$	$-0.33^{+1.02}_{-0.91}$

Table 4. Derived quantities from the best-fit parameter values of the reverse shock.

GRB	080916C	090323	090902B	090926A	110731A	130427A	160625B	180720B
$(t < t_x)$								
$h\nu_{m,r}^{\text{SSC}}$ (GeV)	7.7	4.1×10^2	1.8×10^{-1}	5.9×10^3	1.1×10^{-8}	9.1×10^{-8}	5.8×10^{-4}	2.9×10^{-7}
$h\nu_{c,r}^{\text{SSC}}$ (GeV)	9.3×10^{-2}	1.2×10^{-3}	2.9×10^{-5}	2.2×10^{-6}	1.1	5.5×10^{-6}	1.8×10^{-2}	1.1×10^{-4}
$F_{\text{max},r}^{\text{SSC}}$ (mJy)	1.6×10^{-3}	2.0×10^{-4}	1.3×10^{-1}	2.3×10^{-2}	3.6×10^{-1}	2.7×10	4.7×10^{-3}	3.7
$h\nu_{\text{KN},m,r}^{\text{SSC}}$ (GeV)	4.8×10^2	7.2×10^2	9.9×10	1.0×10^3	8.2	3.2	2.8×10	3.4
$h\nu_{\text{KN},c,r}^{\text{SSC}}$ (GeV)	2.4×10^2	1.5×10	1.2×10	4.5	6.9×10^2	8.9	6.7×10	1.5×10
$(t_x < t)$								
$h\nu_{m,r}^{\text{SSC}}$ (GeV)	7.4×10^{-2}	6.0×10^2	1.1×10^{-1}	5.8×10^2	1.1×10^{-9}	8.3×10^{-9}	7.3×10^{-5}	4.0×10^{-8}
$h\nu_{\text{cut},r}^{\text{SSC}}$ (GeV)	1.6	8.1×10^{-2}	6.1×10^{-3}	8.8×10^{-6}	1.2×10^2	2.0×10^{-4}	1.2×10^{-1}	1.2×10^{-3}
$F_{\text{max},r}^{\text{SSC}}$ (mJy)	1.2×10^{-4}	5.3×10^{-5}	2.1×10^{-2}	5.4×10^{-3}	8.3×10^{-2}	4.4	4.7×10^{-3}	9.7×10^{-1}
$h\nu_{\text{KN},m,r}^{\text{SSC}}$ (GeV)	1.4×10^2	6.3×10^2	9.5×10	6.1×10^2	1.8	2.3	2.8×10	2.3
$h\nu_{\text{KN},c,r}^{\text{SSC}}$ (GeV)	8.8×10^2	3.8×10	7.7×10	1.1×10	2.6×10^3	3.8×10	6.7×10	4.2×10

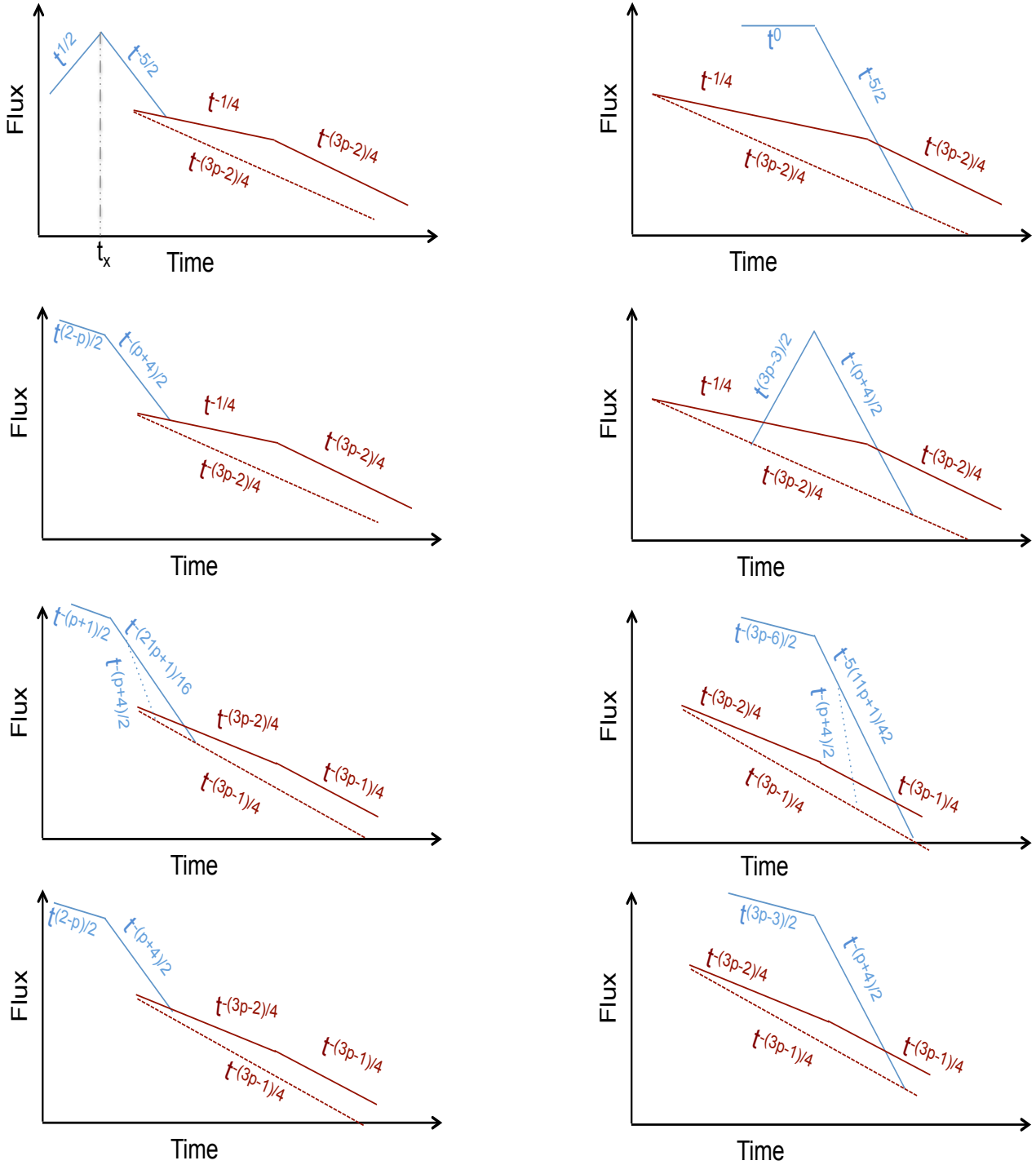


Figure 1. The expected SSC flux from the RS region (blue lines) and the synchrotron flux from the FS region (red lines) when the outflow decelerates in the stellar wind medium. From top to bottom, the panels show the SSC RS light curves for $v_{c,r}^{\text{SSC}} < v < v_{m,r}^{\text{SSC}}$, $v_{m,r}^{\text{SSC}} < v$, $v_{m,r}^{\text{SSC}} < v < v_{c,r}^{\text{SSC}}$ and $v_{c,r}^{\text{SSC}} < v$. The expected SSC fluxes are presented in the thick- (left column) and thin- (right column) shell case. The double-dotted dashed black line corresponds to the shock crossing time. The breaks displayed in the solid red lines are the transitions between $v_{m,f}^{\text{syn}} < v < v_{c,f}^{\text{syn}}$ and $v_{c,f}^{\text{syn}} < v$.

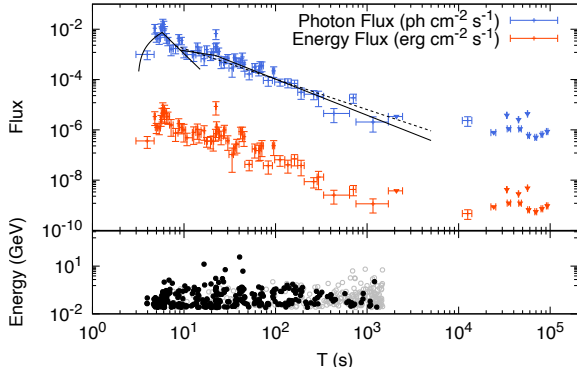
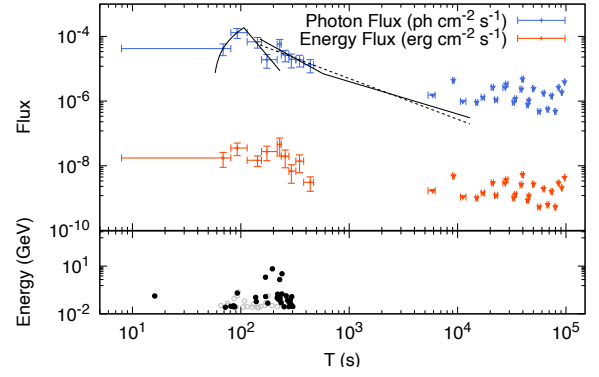
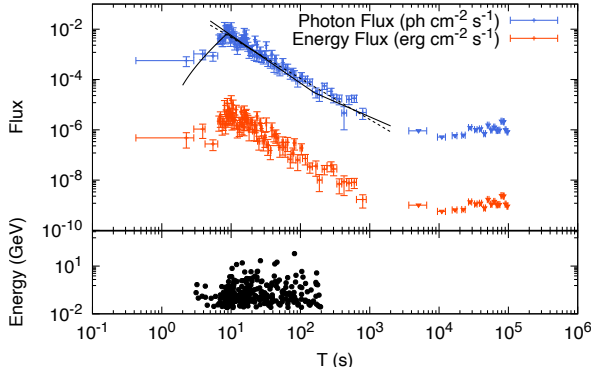
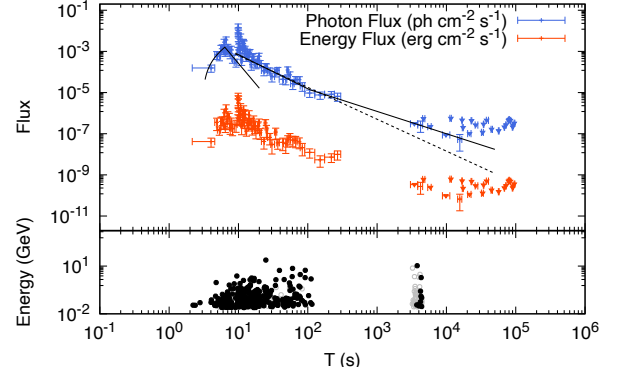
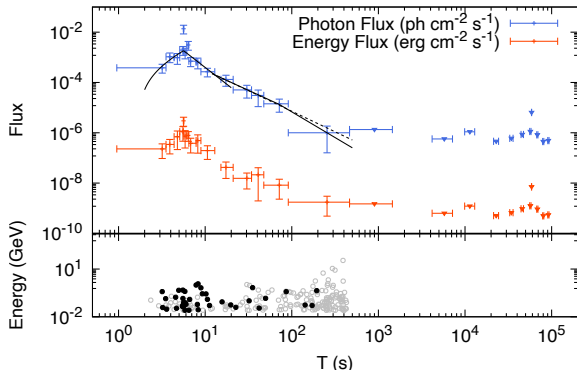
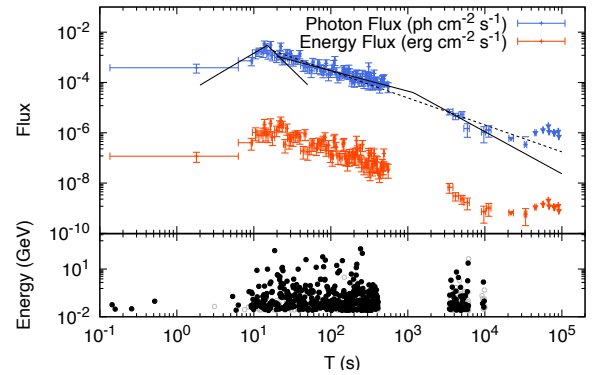
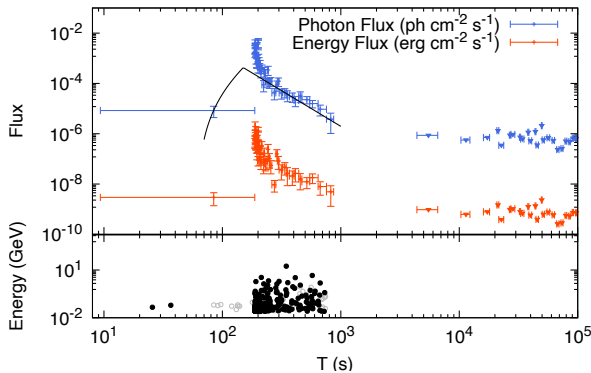
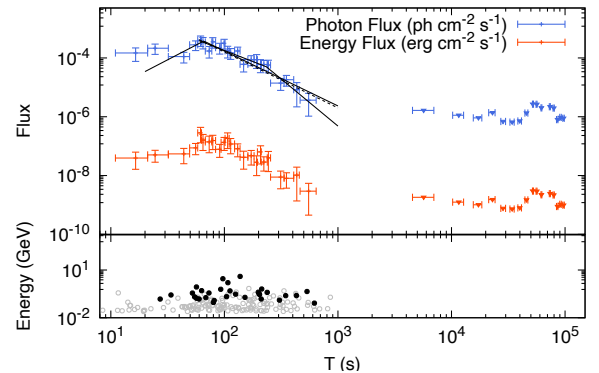

 (a) *Fermi*/LAT light curve for GRB 080916C.

 (b) *Fermi*/LAT light curve for GRB 090323.

 (c) *Fermi*/LAT light curve for GRB 090902B.

 (d) *Fermi*/LAT light curve for GRB 090926A.

 (e) *Fermi*/LAT light curve for GRB 110731A.

 (f) *Fermi*/LAT light curve for GRB 130427A.

 (g) *Fermi*/LAT light curve for GRB 160625B.

 (h) *Fermi*/LAT light curve for GRB 180720B.

Figure 2. The photon flux (blue) and flux energy (red) detected by *Fermi*/LAT are shown in top panels. The photon energy during the entire time window are shown in bottom panels. The filled black dots correspond to a photon with a probability greater than 90% of belonging to the GRB, while the open gray dots correspond to a photon with a probability lower than 90% of belonging to the burst.

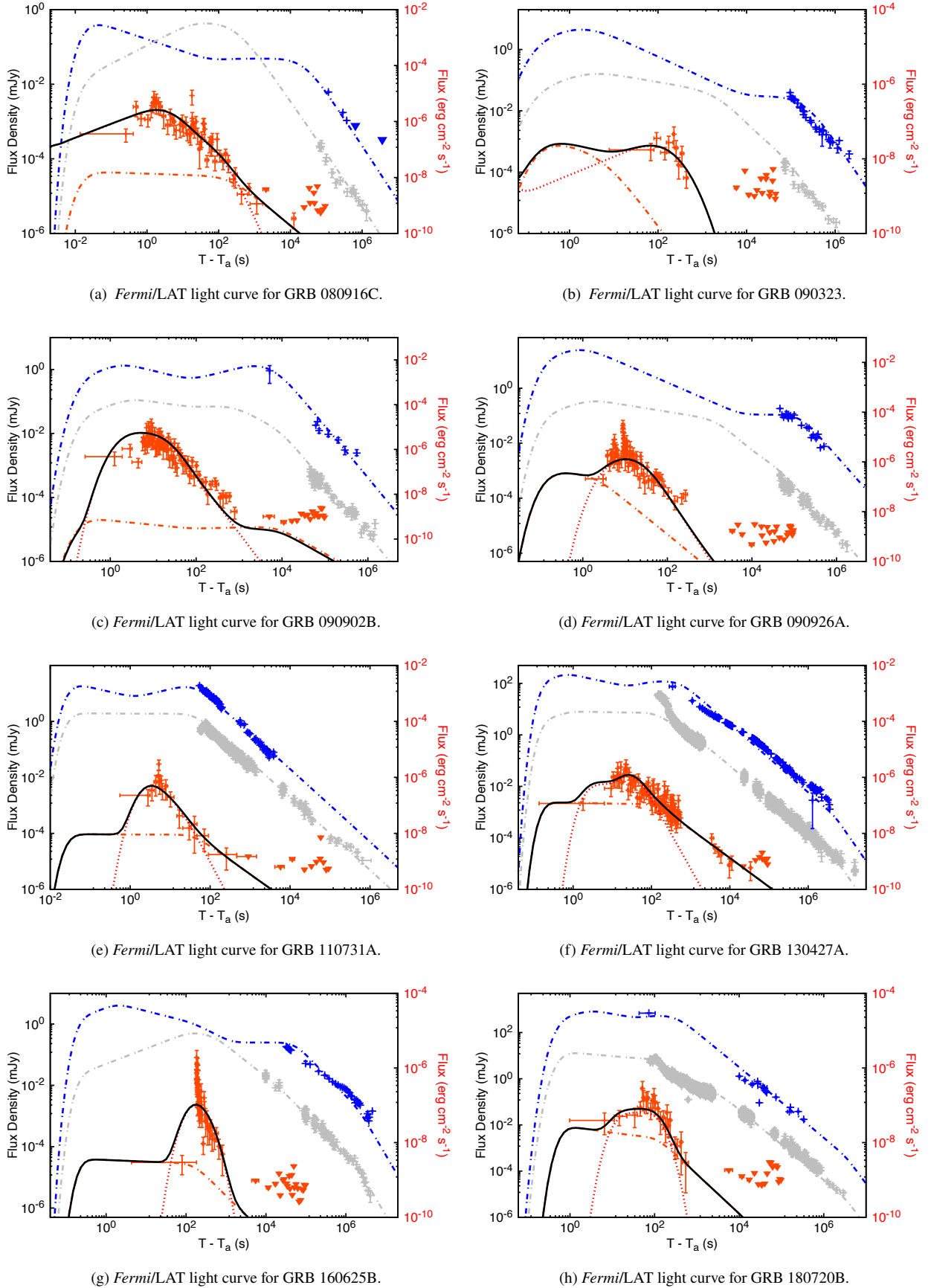


Figure 3. The LAT, X-ray and optical observations of our sample of GRBs with the best-fit curve of the short- (dotted) and long- (dotted-dashed) lasting components. The total emission is displayed with a solid line and T_a corresponds to the starting time obtained from the best-fit parameters listed in Table 1.

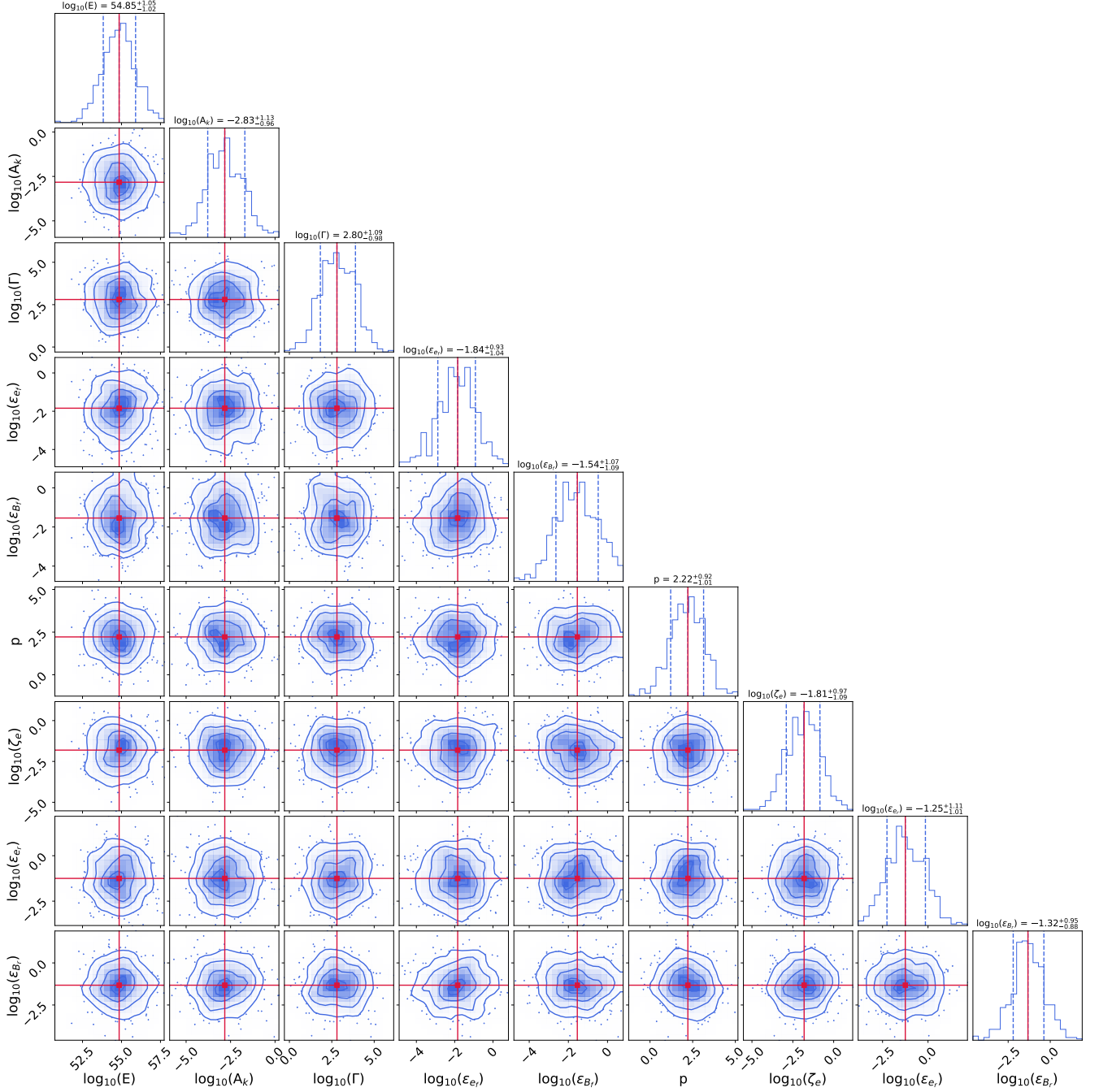


Figure 4. Results of our MCMC parameter estimation are shown in the corner plot for the synchrotron FS and SSC RS model in GRB 080916C. The marginalized posterior densities for each parameter are shown by the histograms on the diagonal, the contours are shown for 1σ , 2σ and 3σ , and the median values in red lines.

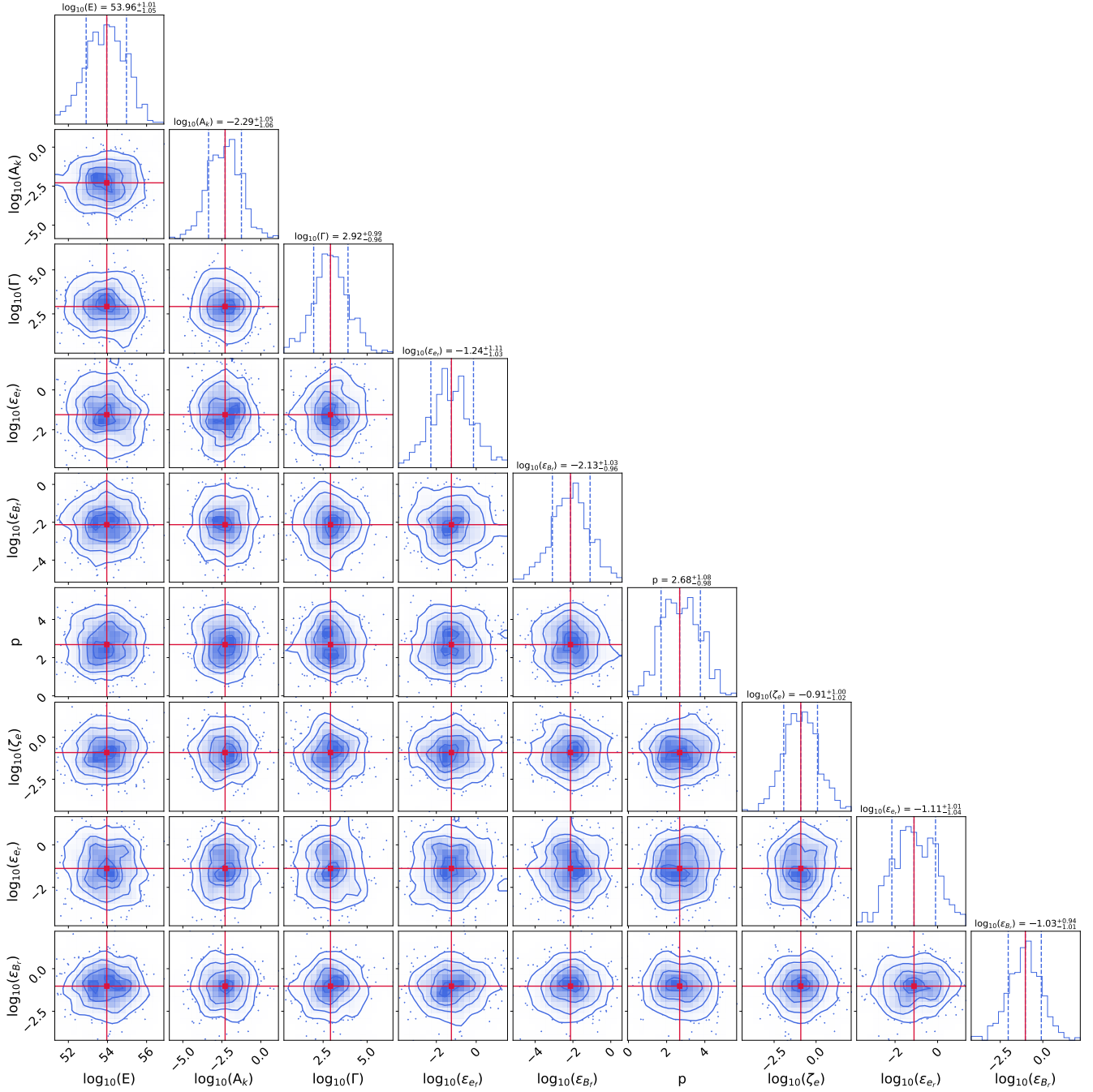


Figure 5. Same as Figure 4, but for GRB 090323.

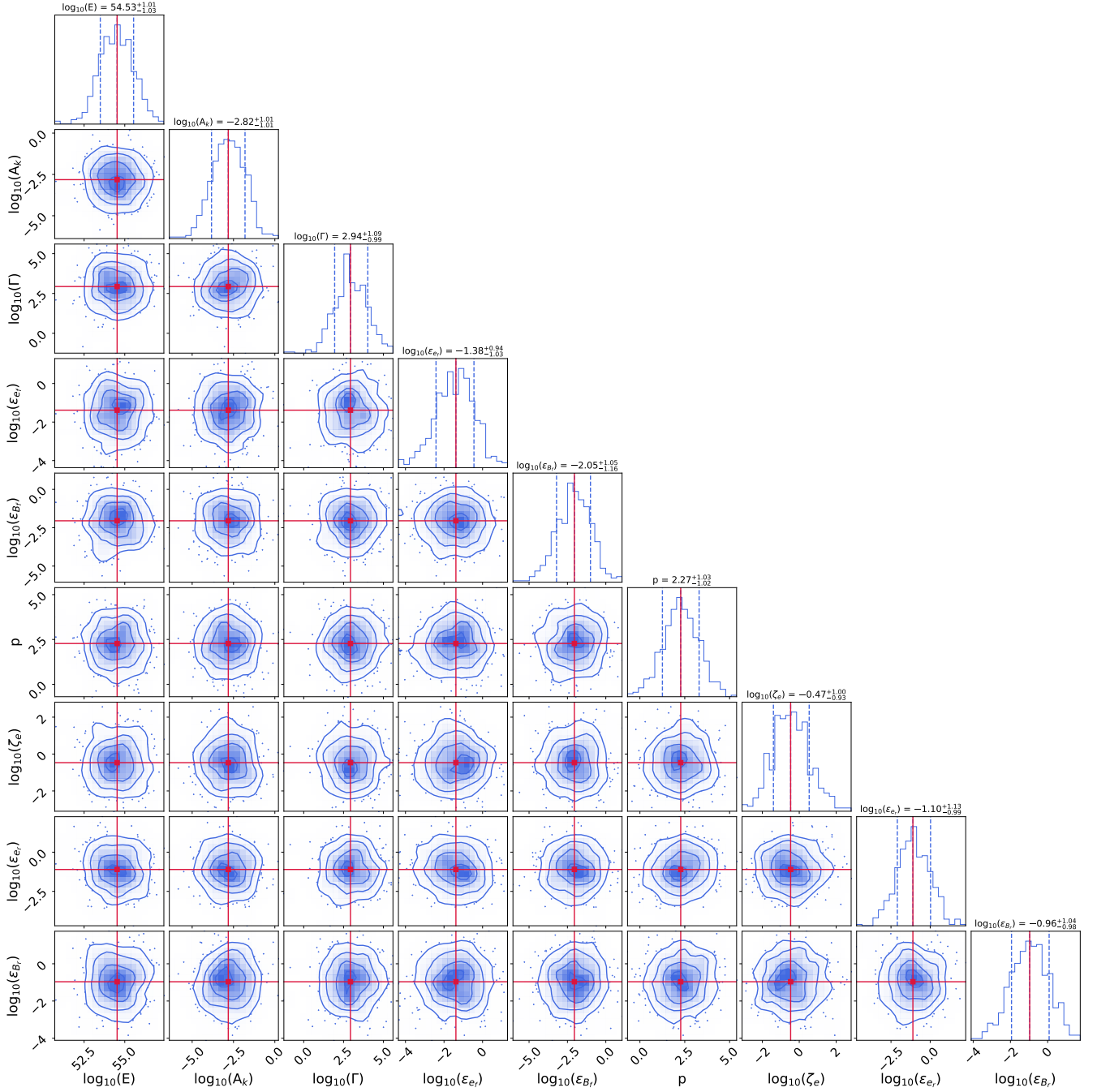


Figure 6. Same as Figure 4, but for GRB 090902B.

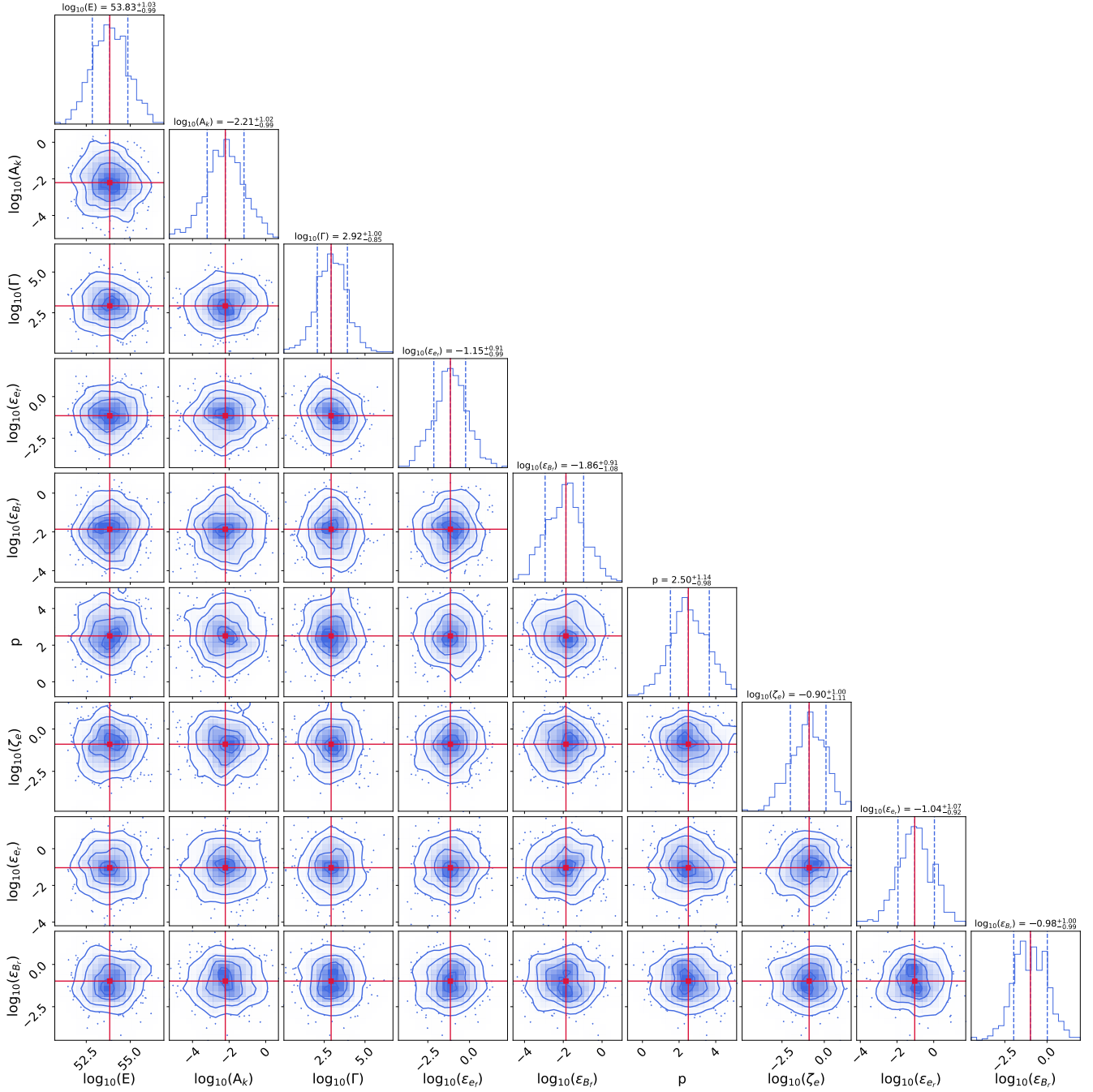


Figure 7. Same as Figure 4, but for GRB 090926A

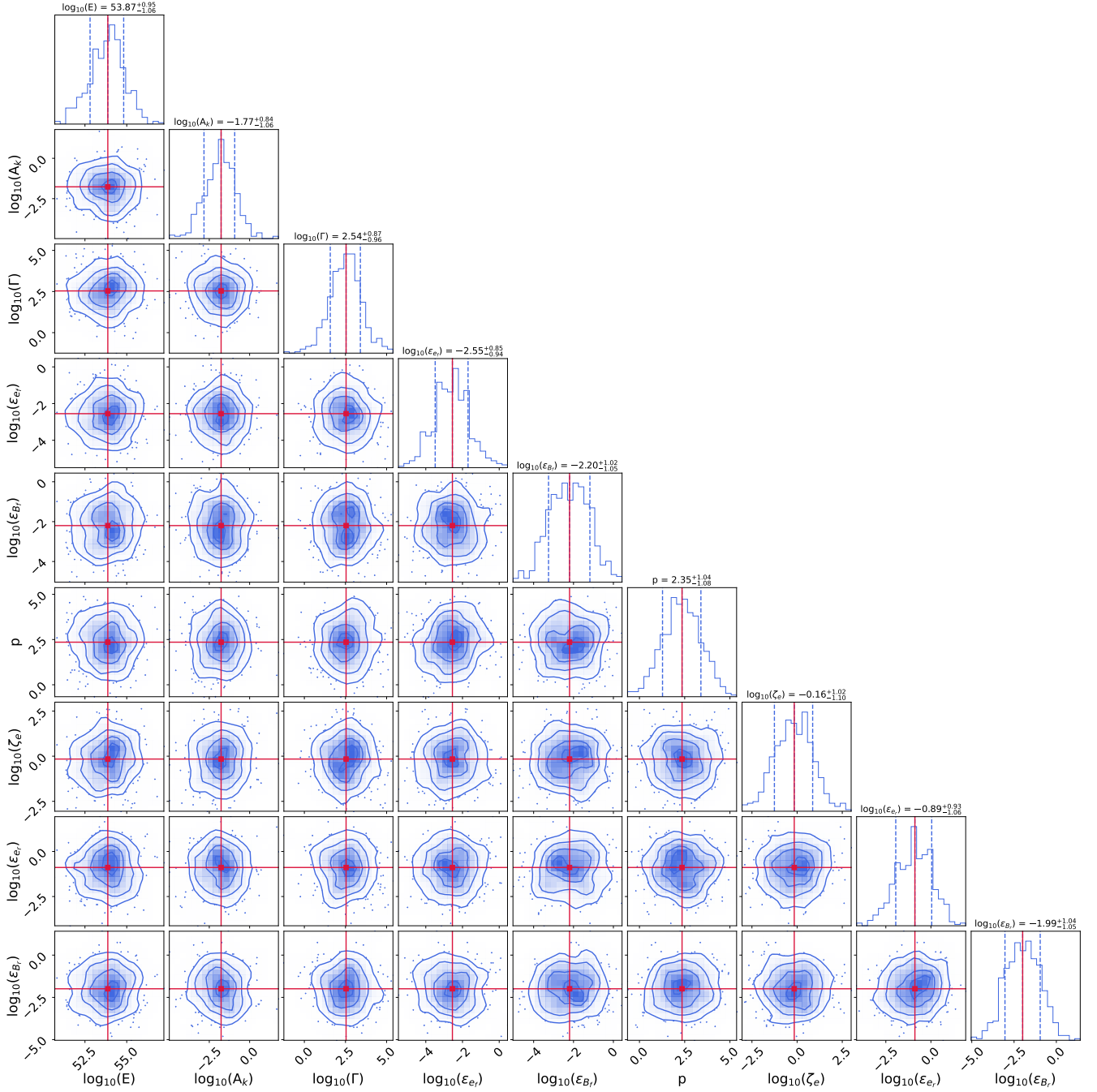


Figure 8. Same as Figure 4, but for GRB 110731A.

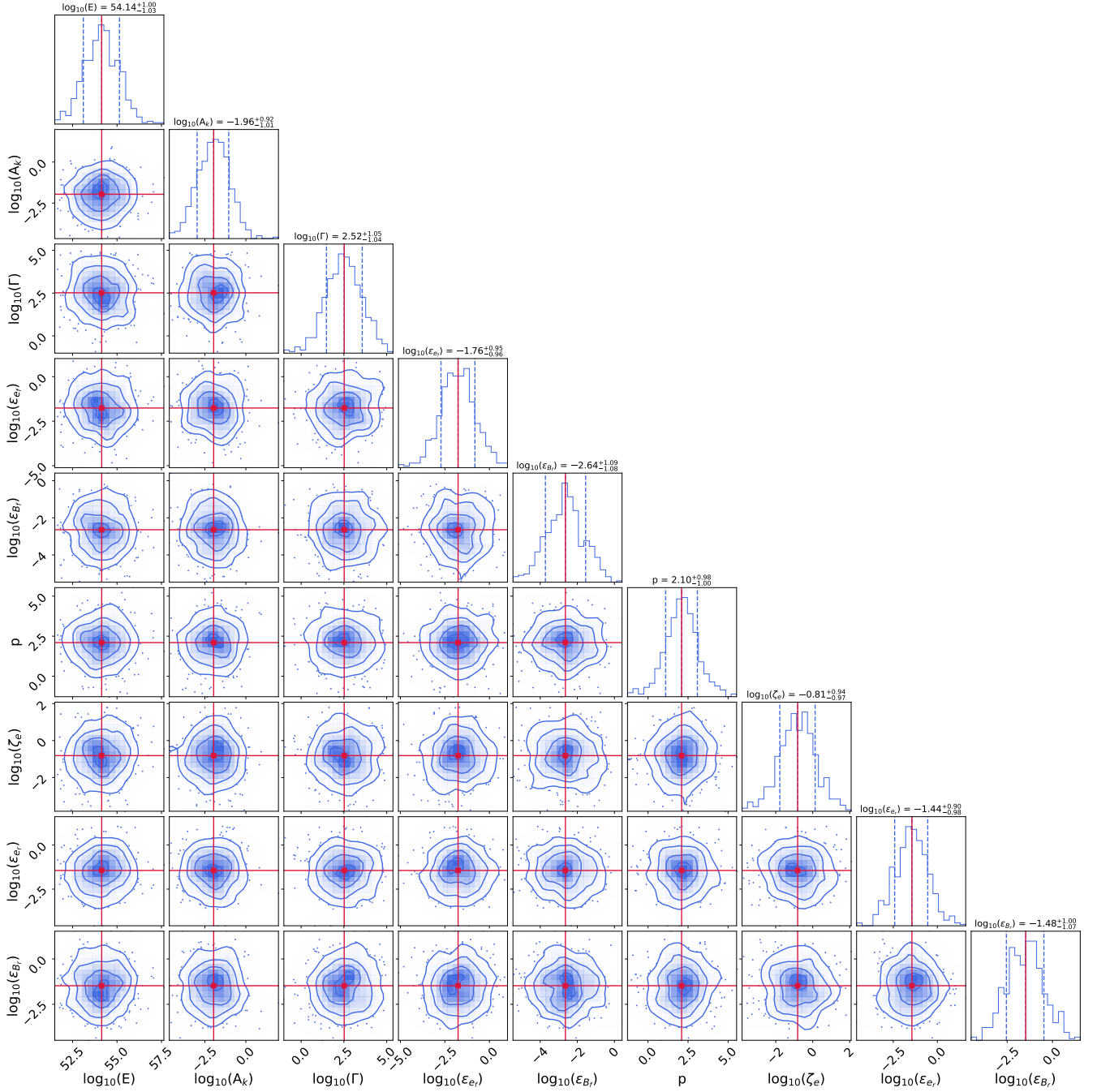


Figure 9. Same as Figure 4, but for GRB 130427A.

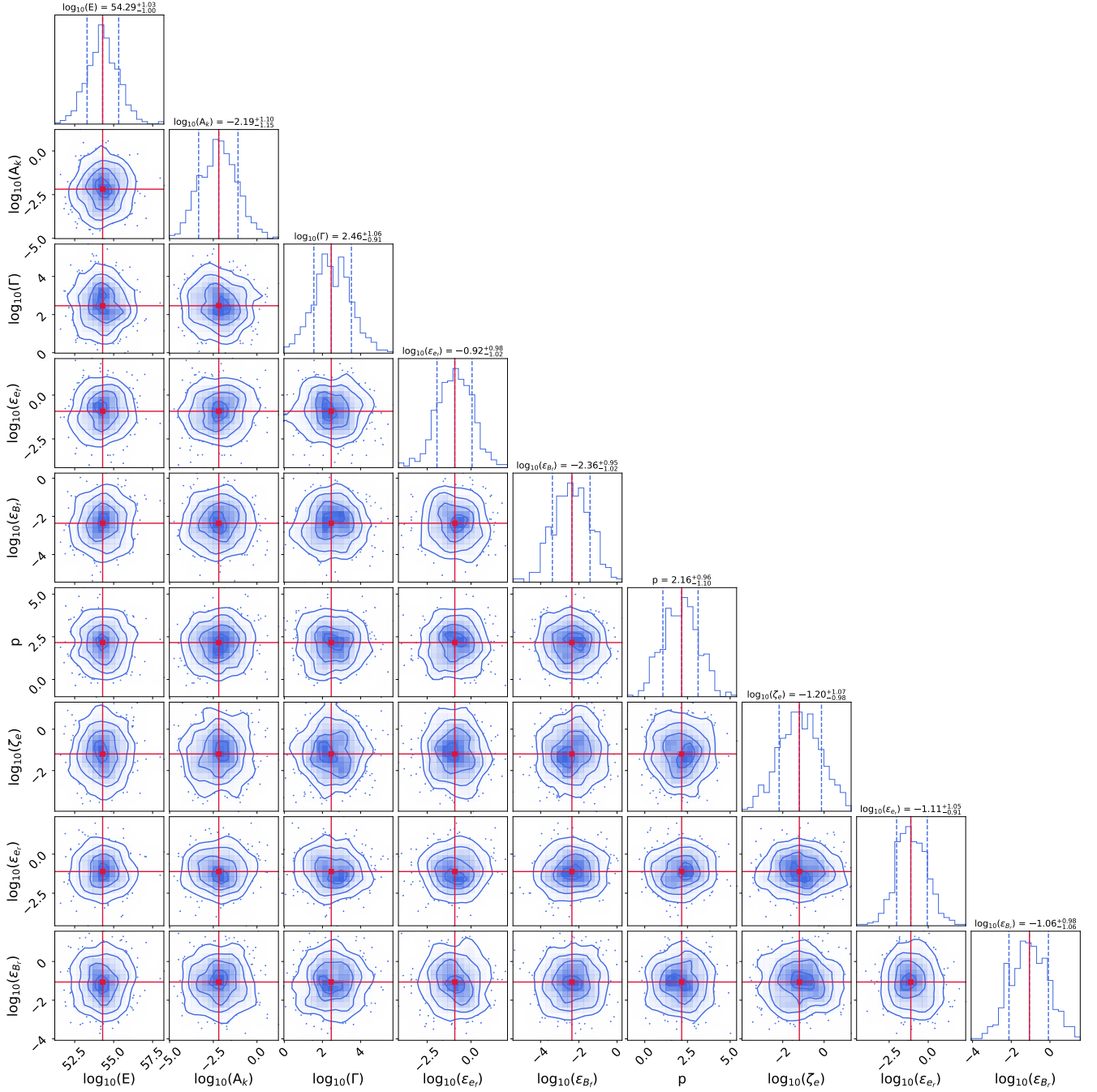


Figure 10. Same as Figure 4, but for GRB 160625B.

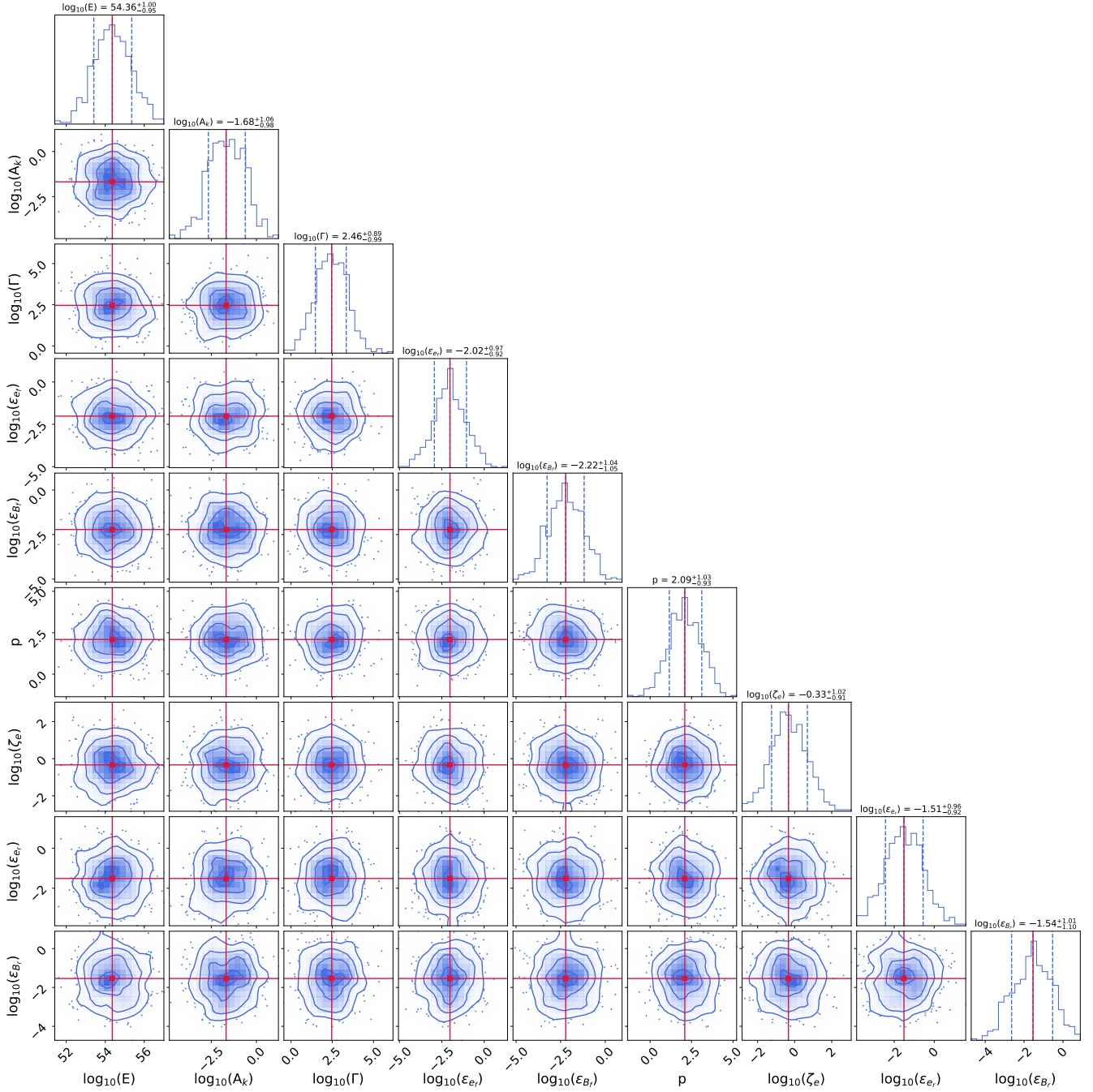


Figure 11. Same as Figure 4, but for GRB 180720B.

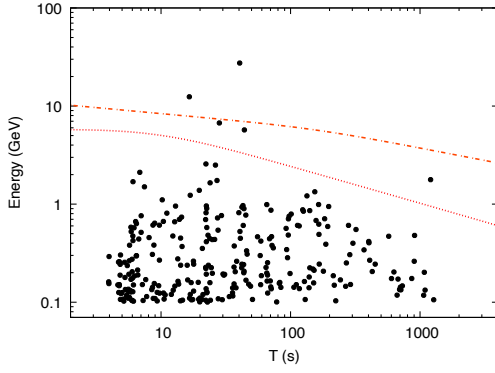
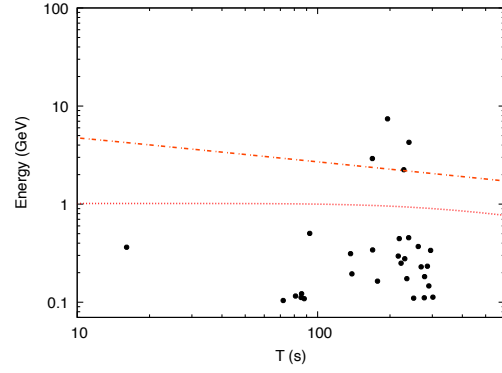
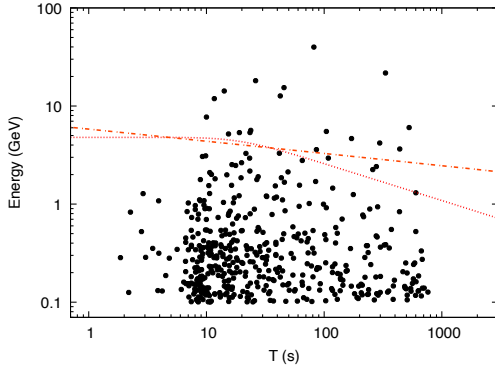
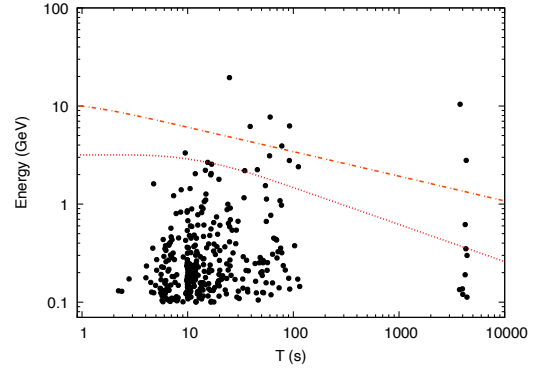
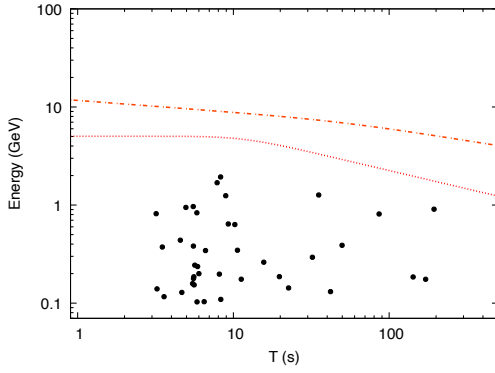
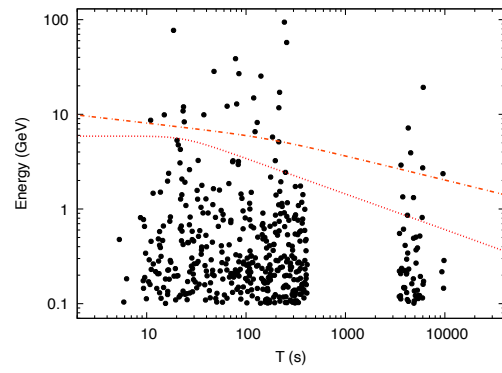
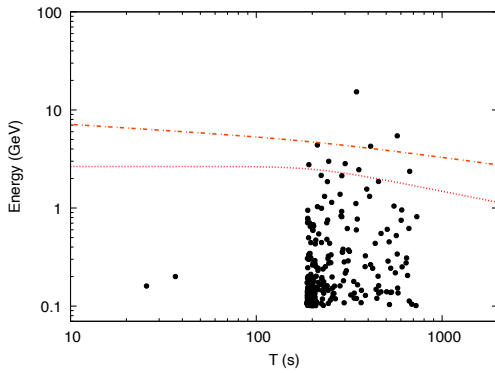
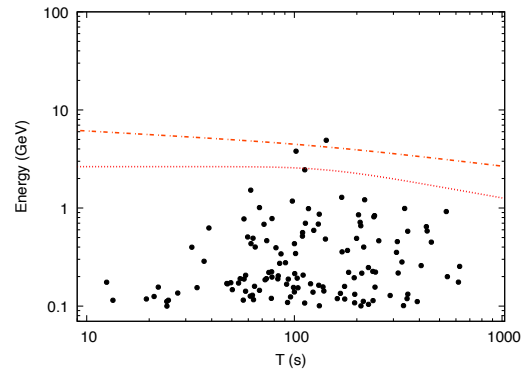

 (a) *Fermi*/LAT light curve for GRB 080916C.

 (b) *Fermi*/LAT light curve for GRB 090323.

 (c) *Fermi*/LAT light curve for GRB 090902B.

 (d) *Fermi*/LAT light curve for GRB 090926A.

 (e) *Fermi*/LAT light curve for GRB 110731A.

 (f) *Fermi*/LAT light curve for GRB 130427A.

 (g) *Fermi*/LAT light curve for GRB 160625B.

 (h) *Fermi*/LAT light curve for GRB 180720B.

Figure 12. All the photons with energies > 100 MeV and probabilities $> 90\%$ of being associated with each burst in our sample. The red lines correspond to the maximum photon energies released by the SSC (dotted) and synchrotron (dashed) from the reverse and forward afterglow model.